Semiannual Report of Progress

THERMIONIC RESEARCH AND DEVELOPMENT PROGRAM

Prepared for
Jet Propulsion Laboratory
California Institute of Technology
4800 Oak Grove Drive
Pasadena, California
Attention: Mr. Fred Abbott
            NASA Procurement Officer
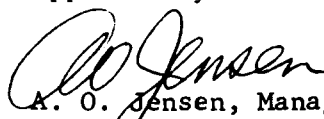
Contract NAS7-514

EOS Report 7118-SA-2   4 August 1967

Prepared by
A. E. Campbell
Project Supervisor

Approved by

A. O. Jensen, Manager
Electro-Optical and
Solid State Technology Division

ELECTRO-OPTICAL SYSTEMS, INC. — PASADENA, CALIFORNIA
A Xerox Company

CONTENTS

ILLUSTRATIONS

ILLUSTRATIONS (contd)

SECTION 1

INTRODUCTION

This is the second semiannual report of progress under Contract NAS7-514, an 18-month program of systematic investigation to improve thermionic converter performance. Thermionic converter performance may be improved by either reducing cesium vapor plasma losses or lowering the collector work function. Examining the plasma losses first, it is assumed that the plasma has been made free of gaseous or solid impurities which could originate from converter structural components or impurities indigenous to the cesium vapor itself. Therefore, the addition of compounds or materials to the plasma should be of a non-contaminating type. Gaseous additives which are added in an attempt to achieve a Penning mixture excitation-ionization action have not been successful since cesium has the lowest known energy level diagram among the abundant elements, nor is there any metastable state of an element which could serve to populate the ion state (molecular or atomic) of cesium. There have also been various schemes of exposing cesium vapor to resonance radiation from a cesium source or pulsing a third element (grid) to produce ions which would diffuse into the interelectrode space. However the absence of significant, long-life performance demonstration from any of these approaches has generally led EOS to the conclusion that plasma losses in a thermionic converter can only be minimized by the proper adjustment of cesium vapor pressure and interelectrode spacing. EOS has investigated the emitter-collector electrode systems of polycrystalline rhenium-rhenium and rhenium-molybdenum over a wide range of emitter temperature (Ref. 1) and established that the maximum voltage output at a fixed current density occurs at a pressure times interelectrode distance, or pd product, of 16.0 ±0.8 mil-torr. The role of the emitter may be characterized as follows:

For a selected emitter tempe_____, the current level desired is strictly a function of the cesium vapor pressure. It has generally been noted that at a fixed emitter temperature, the higher bare work function materials such as polycrystalline rhenium and single crystal (110) tungsten require a lower cesium vapor pressure to achieve a selected current level than the lower bare work function materials such as polycrystalline tantalum or molybdenum. Therefore, the higher bare work function materials allow the use of a lower cesium pressure (for a given current density) and thus allow a wide spacing between electrodes (consistent with an optimum pd of 16.0 ±0.8 mil-torr). Higher current levels can be achieved with these materials at a given temperature and variable cesium pressure, but only at the expense of voltage output.

In summary, it appears that plasma losses can be practically minimized only by achieving the optimum interelectrode spacing-cesium pressure conditions of 16 mil-torr. The emitter material contributes indirectly to converter performance in that it participates in the determination of the spacing between electrodes for given temperature and cesium pressure conditions. The collector, specifically the collector work function, remains to be discussed. There are some simple considerations governing the choice of collector materials which yield low work functions:

    a. The material must be compatible with high pressure cesium and operate reliably for long periods at temperatures from 600°C to 800°C.

    b. For the conditions just described, it should be capable of 10,000 hours life at a constant work function value.

    c. In the case of high temperature (2000°K or greater) emitter operation, the emitter and collector should be of the same material to prevent thin film evaporation and attendant changes in work function; at low emitter temperature (1600-1700°K) operation, a two-material electrode system of the proper materials could be feasible for long life operation.

Coupled with these rules is the simple, empirical experience of thermionic investigators that the highest bare work function materials yield the lowest cesiated work functions and are hence the best candidates for simple cesiated converter collectors. EOS has recently added substance (Ref. 1) to this observation by reporting some interesting precision measurements obtained in both variable parameter test vehicles and converter hardware containing polycrystalline rhenium emitters and polycrystalline molybdenum collectors. Emitter temperature operation of 2200°C for brief periods of time in both instances was sufficient to coat the molybdenum collector surface with a thin layer of rhenium which resulted in an increase in the voltage output in both cases by exactly the difference between the minimum work functions of cesium-on-polycrystalline-rhenium and cesium-on-polycrystalline-molybdenum. The higher bare work function material, rhenium, when employed as a cesiated collector substrate, yields 10-15 percent higher voltage output than molybdenum.

The use of a high bare work function material as a converter collector substrate is one of the central themes of the present EOS thermionic research and development program. Among the state-of-the-art materials, oriented vapor-deposited rhenium appears to possess the most consistently high bare work function. The measurements discussed in Sections 2 and 3 of this report have established, for a limited sample selection, that the bare work function of "oriented" vapor-deposited rhenium is 5.12 ±0.03 eV. The apparatus employed in taking these measurements were guard-ringed devices operated in ultrahigh vacuum systems and utilized precision laboratory means for measuring temperatures, voltages, and electron current. Supporting this effort is a surface work function study of vapor-deposited rhenium utilizing the EOS thermionic emission microscope which was modified to yield high magnification (> 1000X) and allowed high temperature operation (2000°K) of emitter samples while maintaining background pressures of 10^{-9} torr. The results of this study have been both qualitative and quantitative in

nature. Quantitatively, the studies provide emission measurements from individual areas within the grains of the emitter. Qualitatively the study provides electron emission micrographs of high resolution (0.2μ) for observing the phenomenon of secondary recrystallization and the effects on surface work function of various surface preparations such as vacuum heat treatment and electro-etching. Of particular interest during this study was the identification of microstructure within individual grains of vapor-deposited rhenium which sometimes varied in electron emission by an order of magnitude from the rest of the grain. If these intergrain emission measurements can be correlated to an effective work function, the values of work function differ by 0.4 eV from the surrounding grain. The origin and character of this microstructure is presently being studied in more detail, since if it were possible to eliminate or control this surface work function aberration, vapor-deposition surfaces could be optimized to yield work functions closer to single crystal work function values.

Subsequent to the bare work function determination and emission microscope study, these same vapor-deposited electrode samples are being readied for investigation in a variable parameter test vehicle (VPTV) which will measure the performance of these samples in a cesium vapor environment. The VPTV is identical in design and construction to those delivered to the Jet Propulsion Laboratory under JPL Contract 951225. Among the first measurements to be obtained is the minimum cesiated work function of oriented vapor-deposited rhenium. Other measurements will include verification of the optimum cesium pressure-interelectrode distance product data as related to both voltage output at a fixed current level and onset of ionization. Thermionic power output data on a vapor-deposited rhenium electrode system will also be obtained over a wide range of emitter temperatures for optimized cesium pressure, interelectrode spacing, and collector temperatures. The very close-spaced electrode region, near 0.0005 inch and less, will also be

studied to gather further data to augment the theoretical study of the space charge region of the cesium vapor thermionic converter operation. Theoretical development of the double diode behavior at close spacing was presented earlier (Ref. 2) and is reviewed in this report with additional results from a computer solution. In turn, this computer solution is compared to data from the VPTV measurements on the polycrystalline rhenium emitter-polycrystalline rhenium collector system of electrodes. The computer program allows solutions for various combinations of electrode materials, provided their cesiated work functions are known.

SECTION 2

VACUUM EMISSION MEASUREMENTS FROM VAPOR-DEPOSITED RHENIUM

The theory of thermionic emission has been previously reviewed in detail (Refs. 3 and 4). The purpose of this section is to describe the experimental methods utilized in measuring electron emission and obtaining subsequent work function values. Examination of the emission equation

$$J = \frac{I}{S_o} = (1-r) \, AT_e^2 \, e^{-e\phi/kT_e} \tag{1}$$

indicates that two measurable quantities are required to determine the average bare work function, ϕ. These two quantities are the saturated electron current density, J, and the emitter temperature, T_e. The apparent surface area, S_o, is computed from a dimensional measurement. The problem attendant to measuring the saturated electron emission is that of determining the applied electric field which is just necessary to eliminate the space charge barrier and thus achieve the zero-field emission condition. To compensate for this, the zero field emission is determined from an extrapolation of the measured current plotted as a function of the applied electric field in a manner described by Schottky (Ref. 5).

It is experimentally observed that the electron emission from a surface at constant emitter temperature and interelectrode spacing increases rapidly with applied voltage, then levels off and increases linearly with the square root of increasing field. This latter region is generally referred to as the Schottky region and the slope of this line may be extrapolated back to the current axis to obtain the

saturated electron emission at zero field. Applied field strengths generally employed to obtain Schottky emission are in the 10^4 to 10^5 V/cm range. Emitter field strengths on the order of 10^6 to 10^7 V/cm may cause field emission, in which case the thermionic-field emission equations would apply.

The saturated electron emission values obtained from the Schottky plot are used to determine the average work function of the emitting surface by way of a Richardson plot which empirically relates the measured quantities of Eq. 1. The slope of the Richardson line is the value of the average bare work function and the ordinate intercept is the value for the Richardson-Dushman emission constant, A. It has been the experience of workers in the field of electron emission physics that A values are extremely difficult to obtain since extrapolating to the ordinate intercept means transcending several decades of emitter temperatures where little data exists. Further, A values are extremely sensitive to surface contamination which can result from partial pressures of gases, such as O_2 and N_2, in the 10^{-9} torr range. For these reasons, the theoretical value of 120 amps/cm^2 - $^\circ$K^2 is frequently assigned to A and the resulting work function is <u>defined</u> as the effective work function. The typical Langmuir "S" emission plots used to evaluate emitter and collector work functions from cesium-coated surfaces are plots of effective work function computed from Eq. 1 with A set at the theoretical value.

2.1 <u>VACUUM EMISSION VEHICLE (VEV)</u>

The vacuum emission vehicle consists of four major components, emitter sample, electron bombardment heater assembly, collector, and guard ring. Figure 1 shows these components in relation to one another.

RADIATING
FINS (E≈.78)

MOLYBDENUM
COLLECTOR

MOLYBDENUM
BASE

HIGH PURITY (AL 995)
INSULATORS

MOLYBDENUM
GUARD RING

VAPOR-DEPOSITED
RHENIUM EMITTER
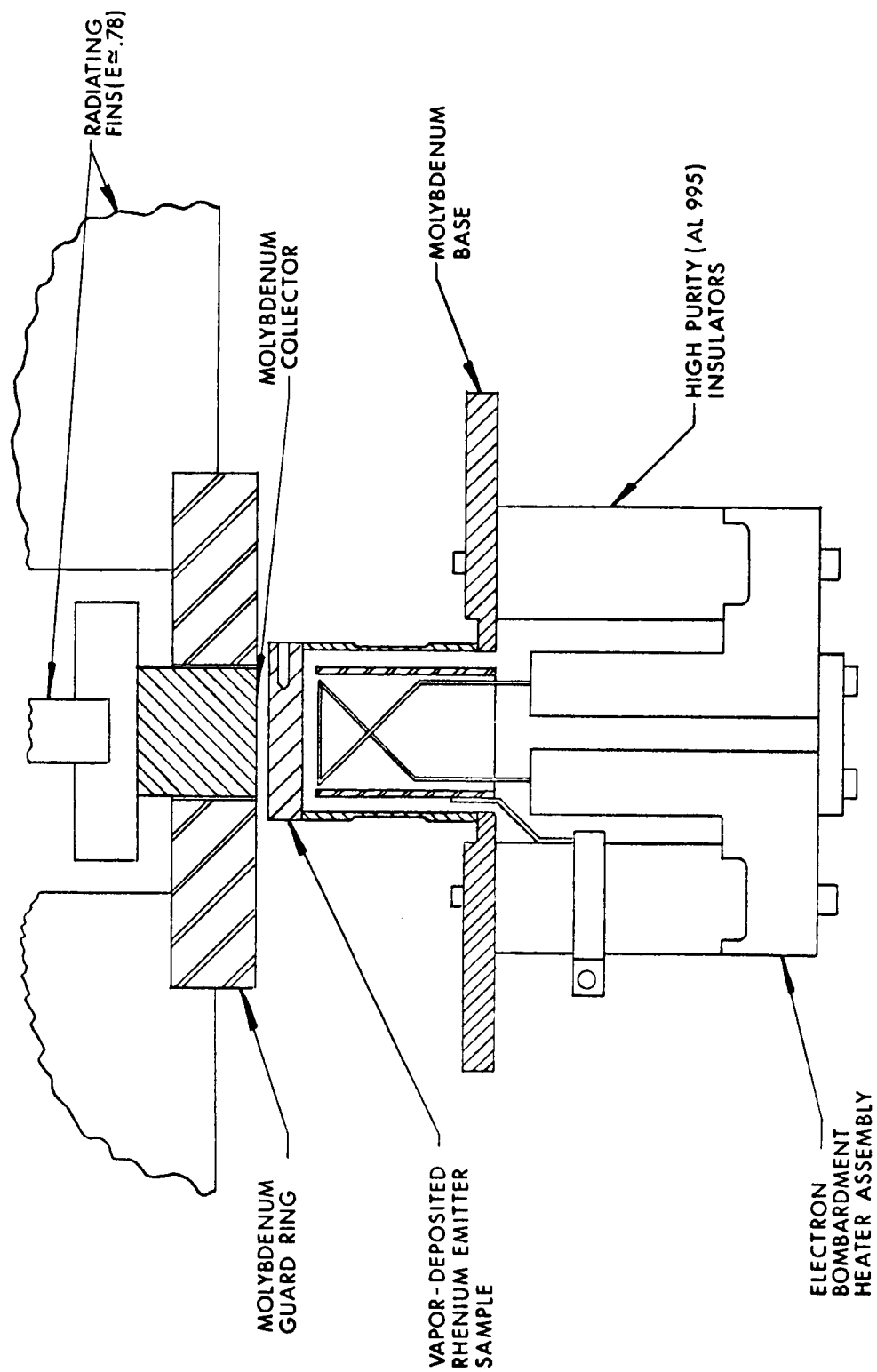SAMPLE

ELECTRON
BOMBARDMENT
HEATER ASSEMBLY

Figure 1. Schematic of Vacuum Emission Test Vehicle

The emitter sample and electron heater subassembly is an integral unit which may be removed and reinstalled by a simple bolting arrangement. The sample can be heated to a temperature of 2400°K without the base temperature exceeding 700°K.

Sample temperatures are measured with a micro-optical pyrometer focused on a 10:1 hohlraum located in the side of the sample, and parallel with the emitting surface. The vapor-deposited rhenium emitter sample is electron-beam-welded onto a rhenium tube which is heat-choked to minimize conduction losses. The tube, in turn, is vanadium-brazed into a molybdenum plate which serves as a holding base for the sample, as well as the electron bombardment gun. Figure 2 shows the collector and guard ring mounted in a stainless steel test fixture. The molybdenum collector is mounted parallel to the sample at a cold spacing of 0.040 ±0.001 inch and intercepts the electron emission from the central 1.83 square centimeters of the 4.0 square centimeter emitting surface. The collector structure includes a radiation fin of approximately 80 square centimeters. The radiating fins are coated with a Rokide "C" coating to adjust its emissivity to 0.78. The collector is heated directly by radiation from the sample and by collected electrons dissipating energy acquired from the applied field between emitter and collector. At the highest voltage and highest current levels, the collector thermal input amounts to over 50 watts which is dissipated by the radiating fin area. The collector surface operates at temperatures less than 500°C.

High purity stand-off ceramic insulators (AL 995), precision ground in length and diameter to 0.0003 inch, are used to provide electrical insulation and to accurately position the collector assembly with respect to both the emitter and guard ring. The molybdenum guard ring is concentric to the collector within ±0.0015 inch, and serves as a guard for the collector surface as well as the collector body. The guard ring which receives heat input in a manner similar to the collector is also provided with radiator fins.
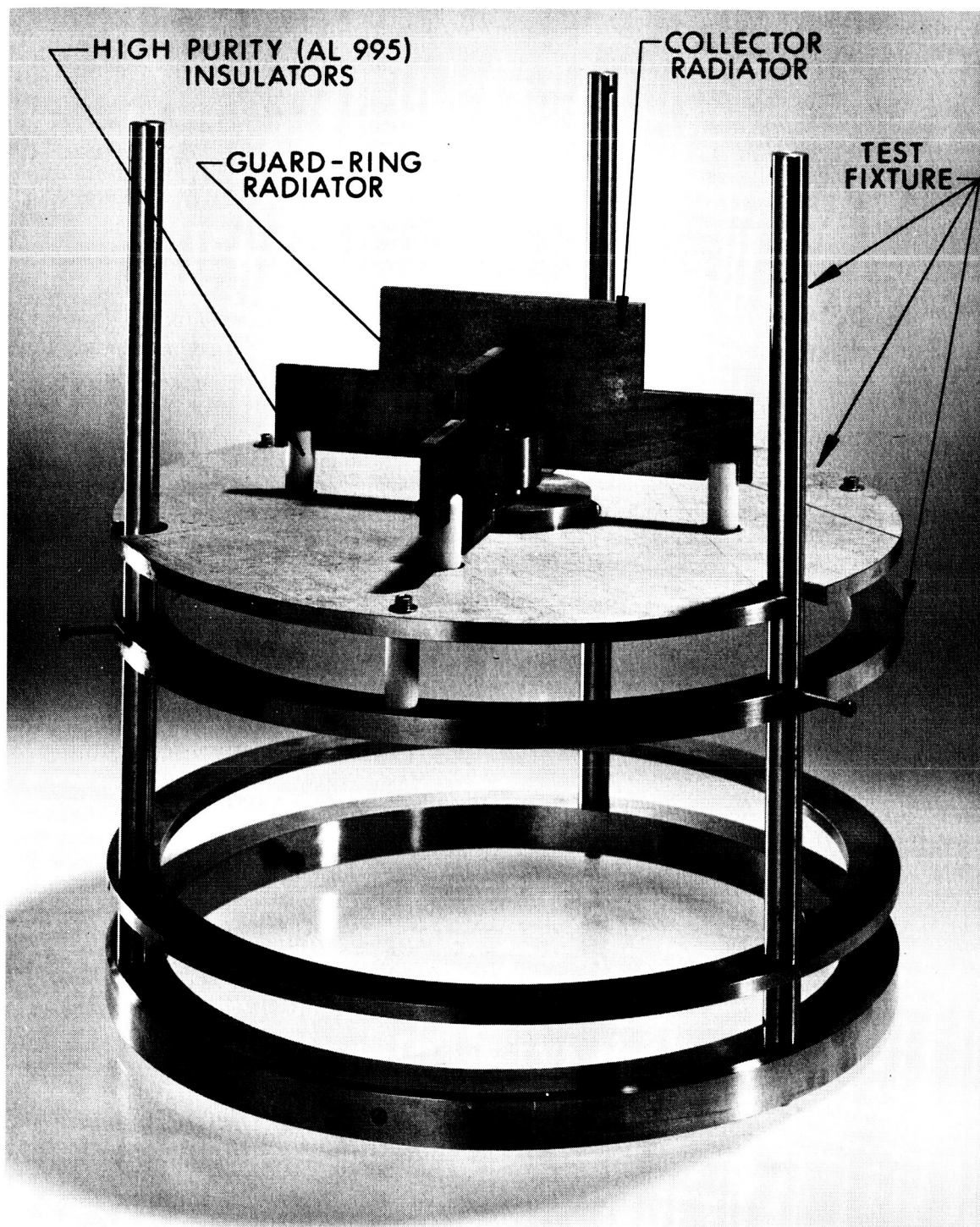
Figure 2. Vacuum Emission Vehicle Mounted in Test Fixture

Figure 3 is the schematic of the electrical test setup for the VEV. A Keithly 610R micro-microammeter is used to measure collector current. It has an accuracy of 3 percent from 3 amperes to 10^{-10} ampere and 4 percent for 10^{-10} to 10^{-13} ampere. A Boonton 95A micro-microammeter (4 percent accurate at 10^{-13}), is used to measure the current flow between the collector and guard ring. In operation the current flow is maintained two to three decades below the current level measured in the collector circuit. For practical purposes, the potential of the guard ring under these conditions is considered to be equal to that of the collector. All emission measurements were taken in a vac-ion pumped environment at pressures of 4 to 9 x 10^{-8} torr after the test fixtures, emission vehicle components, and vacuum bell jar were thoroughly baked out. Two Fluke model 408B power supplies were used to maintain and adjust the potentials of the collector and guard ring. The output of these supplies is adjusted by a precision Kelvin Varley divider, providing an accuracy of 1/4 percent and resetability of 0.1 percent.

The emitter sample temperature measurement is repeatable, by experienced operators, within $\pm 3^{\circ}K$. The absolute determination of temperatures in the $2000^{\circ}K$ to $2500^{\circ}K$ range is $\pm 7^{\circ}K$, a value consistent with the Bureau of Standards certification of strip-filament lamps (Ref. 6). EOS micro-optical pyrometers have been continuously checked and calibrated against these lamps for a period of five years without any detectable variation. In addition, corrections for the photon transmission loss through Pyrex viewing windows were determined as shown in Table I.

The combined experimental accuracy for determining work function values from the experimental measurements of current, temperature, and area are estimated to be ± 0.04 eV.
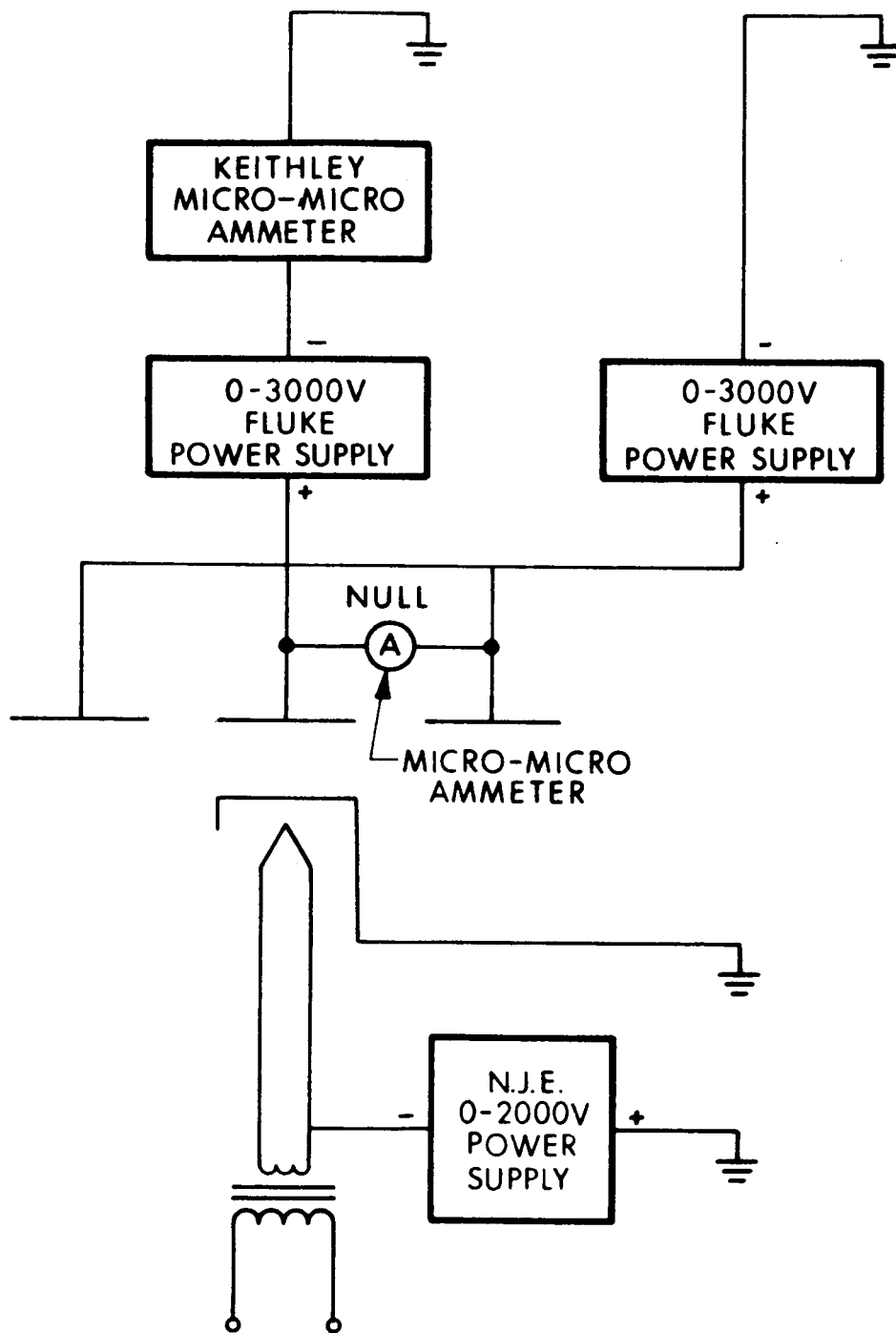
Figure 3. Schematic of Electrical Instrument for
Vacuum Emission Vehicle

TABLE I

TRANSMISSION CORRECTIONS
FOR MICRO-OPTICAL PYROMETER MEASUREMENTS

True Temperature $^{\circ}C$	ΔT (Transmission Loss Through 12 in. Diameter Bell Jar)
1227	13
1427	16
1627	19
1905	23

2.2 EFFECTIVE WORK FUNCTION EVALUATION (A = 120 AMPS/cm^2-$^{\circ}K^2$) OF VAPOR-DEPOSITED RHENIUM

The electron emission from four vapor-deposited rhenium samples was measured in the vacuum emission vehicle utilizing those instruments and methods as described in the previous section. The average effective work function of these samples is listed in Table II. The following paragraphs describe some of the experimental particulars employed to determine those work function values.

2.2.1 VAPOR-DEPOSITED RHENIUM SAMPLE I

Electron emission measurements were taken from Sample I at six emitter temperatures in the range of 1940°K to 2350°K. At each temperature the emission was measured as a function of the applied voltage between the emitter and collector to establish the Schottky line. Applied voltages from 1 volt to 3 kilovolts were used to obtain these measurements, although it was found that the Schottky line could be adequately determined from applied voltage levels of 1 kilovolt. Since the Schottky line is used to obtain the field-free, or saturated emission, from which the work function is determined, it was critically important to maintain a constant emitter temperature and electric field during

TABLE II

SUMMARY OF EFFECTIVE WORK FUNCTION, ϕ_{eff},[*]

VAPOR-DEPOSITED RHENIUM SAMPLES

Emitter Temp °K	Sample I	Sample II	Sample III	Sample IV
1698	(5.05)	5.09	--	--
1792	(5.06)	5.12	--	--
1855	(5.07)	5.12	--	--
1857	5.08	--	--	--
1876	--	--	5.07	--
1943	--	--	5.07	5.12
1947	5.06	--	--	--
2003	(5.08)	5.13	--	--
2008	5.08	--	--	--
2046	--	--	5.09	5.14
2051	(5.08)	5.15	--	--
2096	--	--	--	5.13
2105	5.08	5.16	5.10	--
2150	--	5.14	--	5.15
2160	--	5.10	--	--
2195	--	--	--	5.17
2205	--	5.11	5.13	--
2262	5.09	5.15	--	--
2336	5.10	5.15	--	--

[*]Estimated ϕ_{eff} ±0.04 eV, as discussed in Subsection 2.1

the measurements. Consequently, before each set of data was taken, all components of the emission vehicle were allowed to reach a steady-state temperature. In this manner thermal expansion of the emitter subassembly and collector subassembly and mounting fixture was held constant for an established emitter temperature.

The effective work function was calculated from the expression

$$\phi_{effective} = (1.98 \times 10^{-4}) \, T \log [120 \, S_o T^2 / I(0)] \qquad (2)$$

where S_o is the emitter area (in square centimeters) defined by the collector-guard ring geometry; T is the emitter temperature (in ^oK); and I(0) is the zero field saturated emission in amperes. The constant, 1.98×10^{-4}, is appropriate for $\phi_{effective}$ in units of electron volts and for logarithms to the base 10.

The solid line in Fig. 4 was drawn through the experimental data points and resulted in a measured slope within 1.7 percent of the theoretically predicted value. Other Schottky plots yielded similar agreement between measurements and theory.

Each zero-field emission current value at a given temperature was also used to construct a Richardson plot as shown in Fig. 5. From the slope of the line the Richardson work function is measured to be 4.93 eV. The Richardson intercept A_R is 49 $A/cm^2 (^oK)^2$.

Since the Richardson line and the effective work function value are merely alternate ways of presenting the same experimental data, there is a relationship between the effective work function, sample temperature, Richardson work function, and Richardson intercept. These parameters are related by

$$\phi_{effective} = \phi_R + kT \ln(120/A_R) \qquad (3)$$

where ln designates Naperian logarithms. Converting to base ten logarithms, this expression can be written

$$\phi_{effective} = \phi_R + 1.98 \times 10^{-4} \, T \log (120/A_R) \qquad (4)$$
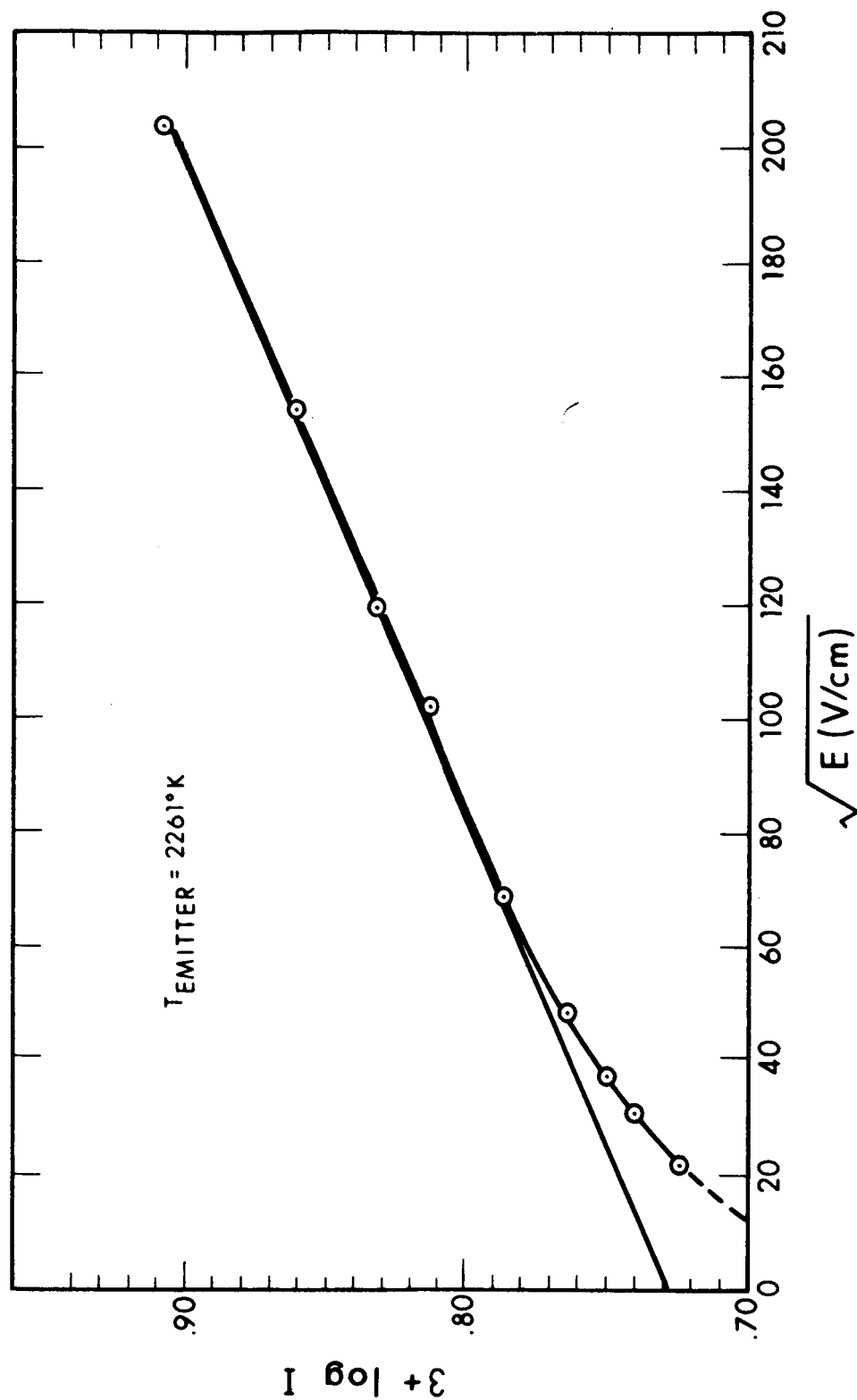
Figure 4. Schottky Plot of Emission from Vapor-Deposited Rhenium Sample I, at an Emitter Temperature of 2261°K
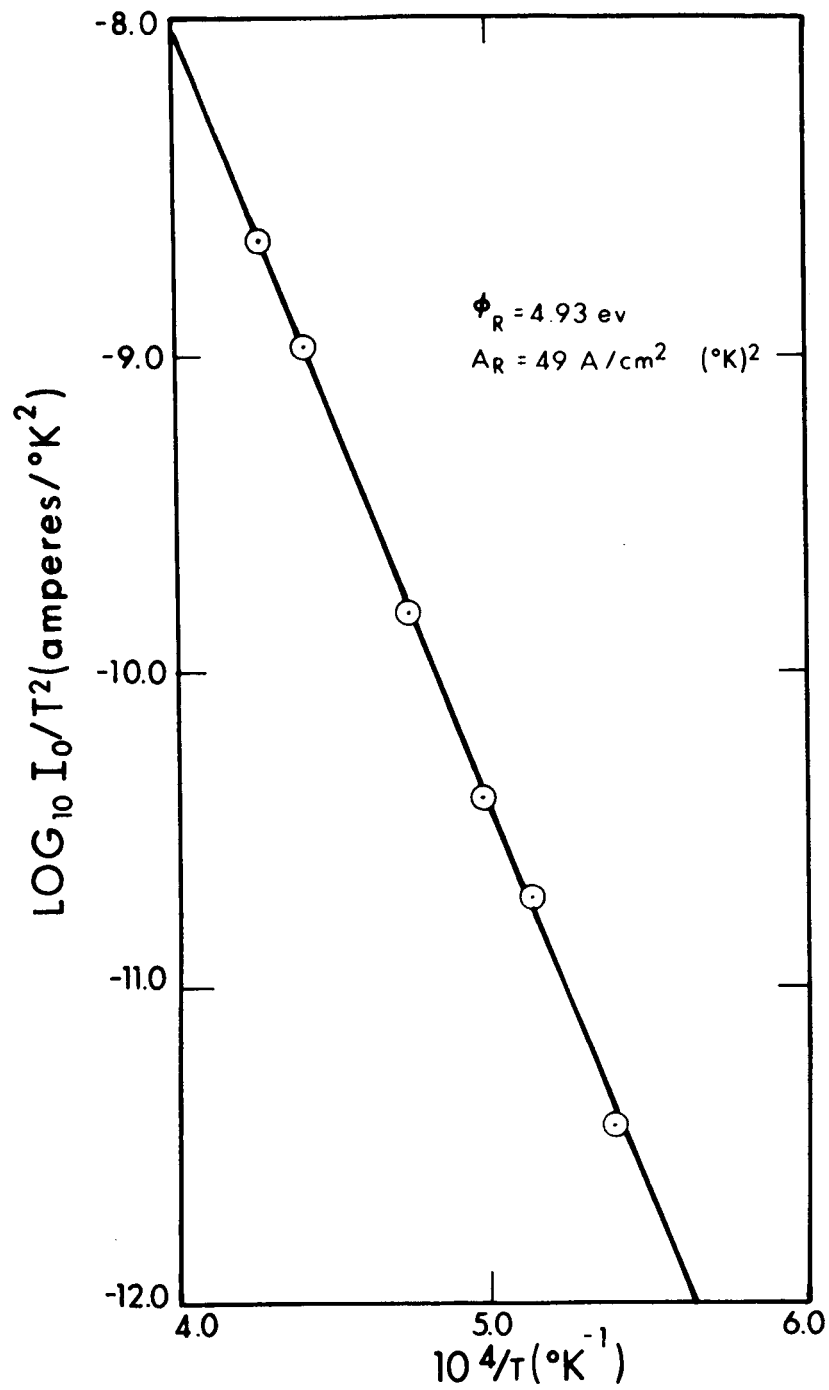
Figure 5. Richardson Plot for Vapor-Deposited
Rhenium Sample I

for work functions in units of electron volts, and A_R in $A/cm^2 (^{\circ}K)^2$. Thus, using the experimentally determined Richardson work function and intercept, $\phi_{effective}$ should vary linearly with temperature according to the above equation if the data analysis is consistent.

Figure 6 is a plot of effective work functions for Sample I versus temperature. The solid line in this figure is computed with the ϕ_R and A_R determined from the Richardson plot in Fig. 5. The effective work functions shown in parentheses in Table II were obtained from the line of Fig. 6.

2.2.2 VAPOR-DEPOSITED RHENIUM SAMPLES II, III, AND IV

The electron emission data obtained from Samples II, III, and IV were analyzed and computed in accordance with the preceding discussion on Sample I. The effective work function values recorded for all samples varied a total amount of ±0.04 eV about the median value of 5.12 eV (see Table II). Variations in the linearity of the Schottky plot seen at EOS were similar to variations that have been predicted (Ref. 7) and investigated by other observers (Ref. 8). A typical example of these variations is shown in Fig. 7.

2.3 EFFECTS OF ELECTRO-ETCHING

Sample II was selected to ascertain whether the effective work function of vapor-deposited rhenium could be altered by electro-etching. Figure 8 is a metallographic photo taken at 500X of the vacuum heat treated vapor-deposited rhenium surface before electro-etching. In addition to the initial heat treatment of 2300°C for 1 hour, the sample had been operated at 1900°C for 40 hours.
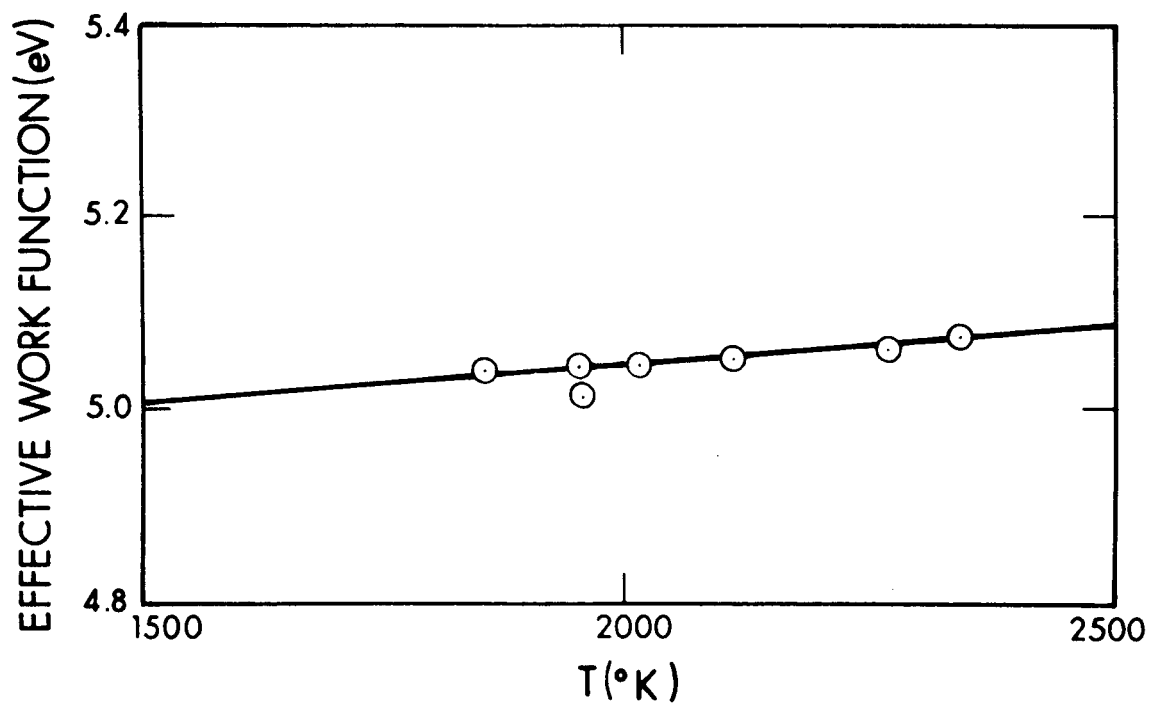
Figure 6. Effective Work Function versus Emitter Temperature
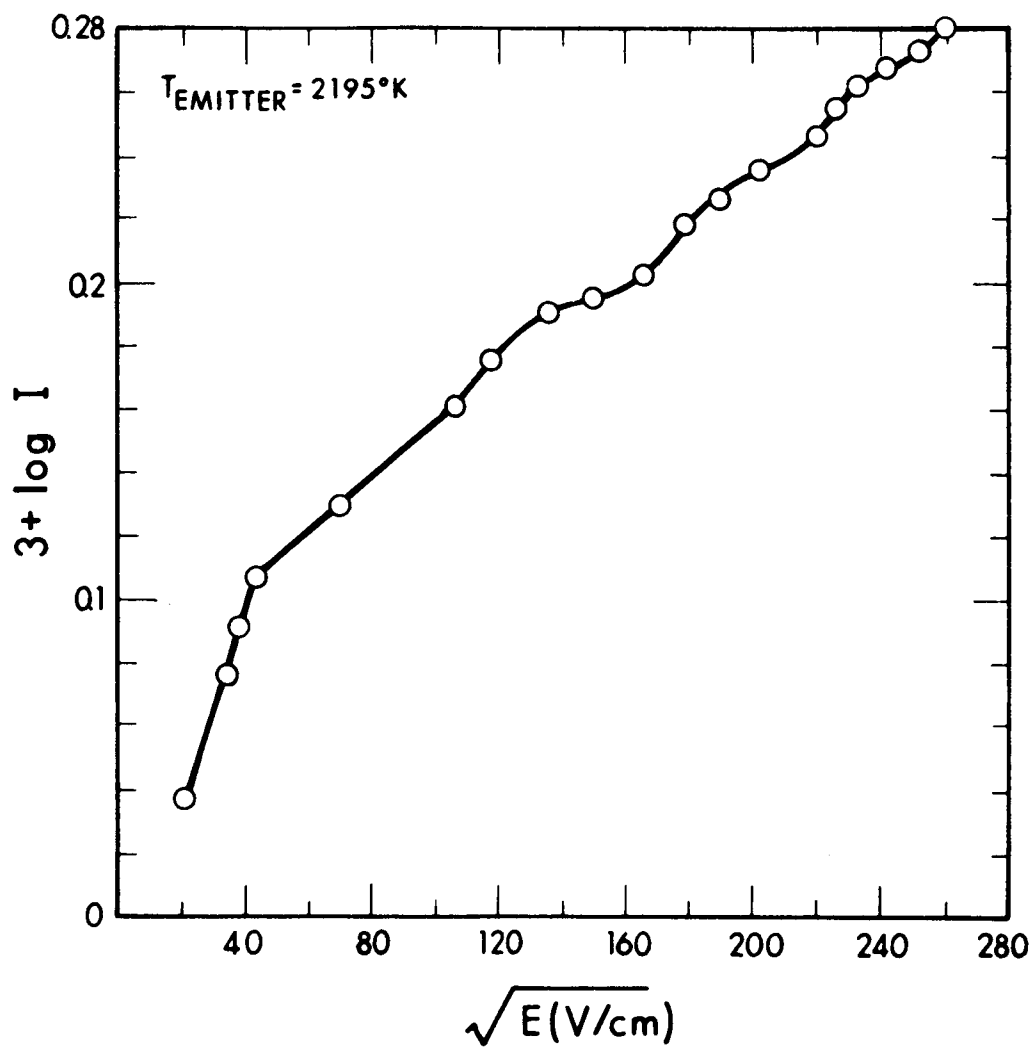
Figure 7. Periodic-Type Variations in a Schottky Plot of Electron Emission
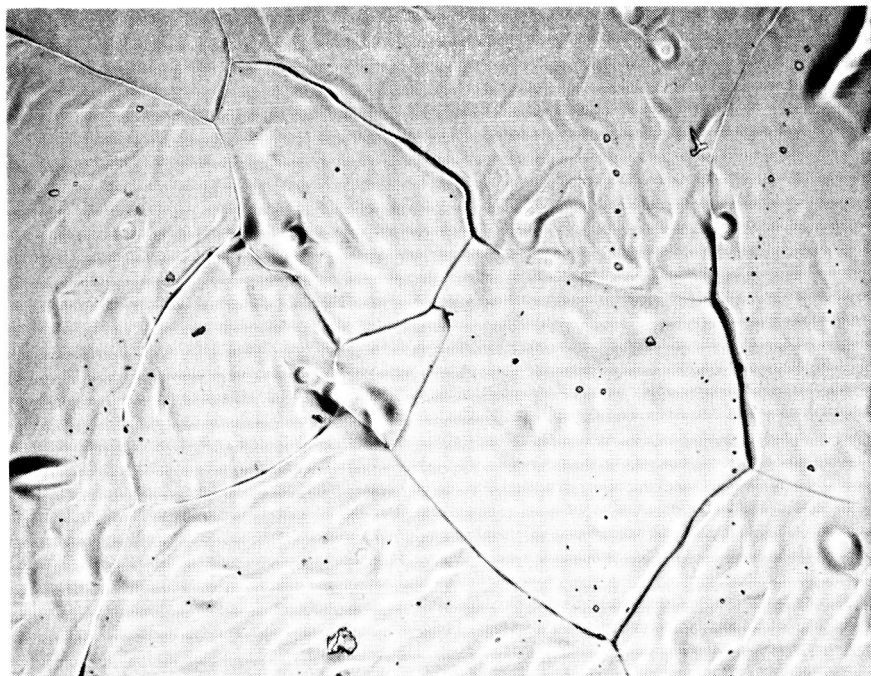
Figure 8. Photomicrograph of Vapor-Deposited Rhenium
Sample II after Vacuum Heat Treatment at a
Temperature of 2300°C for 1 Hour, Subsequent
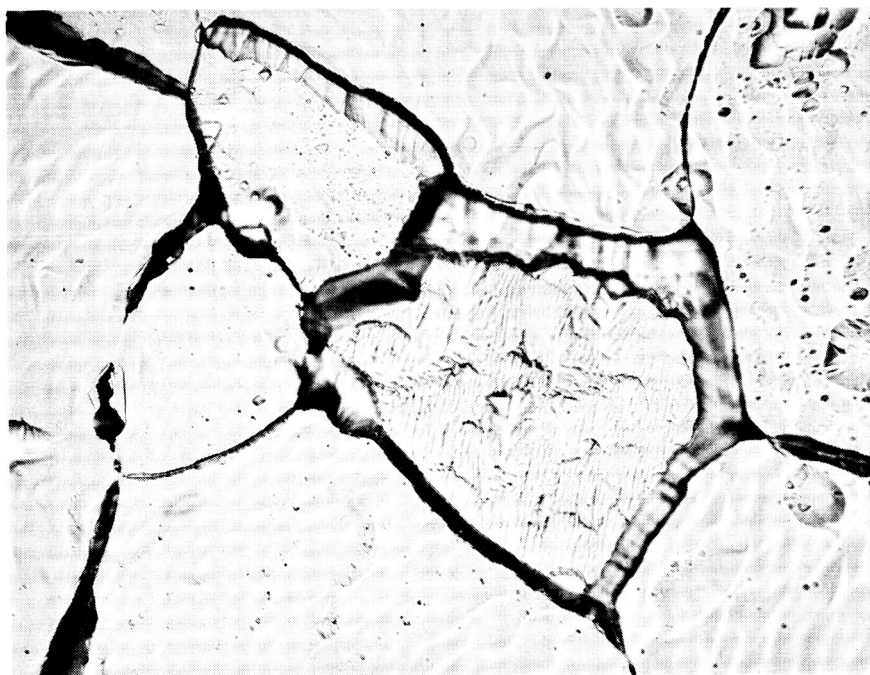Operation at Approximately 1900°C for
Approximately 40 Hours

Figure 9. Photomicrograph of Vapor-Deposited Sample II
after Electroetching (see Fig. 8 500X)

P0331

Sample II was electro-etched with the vapor-deposited rhenium as the anode in an electrolytic solution of 350 ml perchloric acid, 175 ml methanol, and 50 ml butoxyethanol. A rhenium rod was used as a cathode. A potential between 2 to 5 volts was used, with a current density of approximately 0.1 A/cm^2. The electrolytic bath was stirred constantly and the temperature was maintained at approximately 20°C. Figure 9 is a metallographic photo of this same surface after electro-etching operation. As expected, the removal of rhenium from the surface was not uniform. This process transformed the surface, which was initially smooth in appearance, to a jagged surface bound by sharp edges. Grain boundaries were excessively etched and etch pits were observed. The relative heights of the grains changed, some well below those of neighboring grains.

This same sample was then tested in the vacuum emission vehicle to determine if the emission characteristics had been altered by this process. No change was observed in the saturated electron emission; in fact, at each reproduced emitter temperature, measured currents as a function of applied field were identical to the "before-etched" condition.

SECTION 3

ELECTRON EMISSION MICROSCOPE

Electrons, thermionically emitted from a specimen metal at high temperatures, can be used to provide a magnified image of the specimen surface by accelerating them through an electrostatic lens system and focusing them on a phosphor screen. An imaging device designed for this purpose is called a thermionic electron emission microscope.

A thermionic emission microscope is normally operated so that the light intensity emitted by a region of the image on the phosphor screen is proportional to the electron current emitted by the corresponding region of the specimen surface. Thus the pattern displayed by the image and the contrast in the pattern are the result of selective electron emission from the specimen. Since the electron emission from a region of the specimen surface is determined by the local electron work function, the pattern displayed by the image is basically the work function pattern of the specimen surface.

The work function pattern is due to the distribution of exposed crystal faces developed within the surface grains. Each face of a crystal has a characteristic work function, and those exposed on the specimen surface appear in the emission image with an intensity inversely related to their work function values, i.e., high work function faces appear as low intensity regions and low work function faces as high intensity regions. Surface microstructure is made visible by the work functions of vicinal faces developed in irregularities of the surface.

3.1 MICROSCOPE DESIGN AND OPERATION

It was anticipated that many of the vapor-deposited rhenium grains would have dimensions as small as 0.002 inch or less. This was known to be true, at least, for heat treated vapor-deposited tungsten. Based on these considerations, a microscope magnification of 1000X was selected to present a readily discernible image on a 3-inch-diameter screen. In conjunction with this, it was felt desirable to have a resolution of 0.1μ to 0.2μ so that microstructure within an individual grain could be examined. Having established these criteria, a modification of the EOS emission microscope required:

    a. A two-lens system to achieve a minimum of 1000X magnification.

    b. A 30 kV accelerating potential to achieve 0.1μ resolution.

    c. A high temperature grid and grid support system to permit emitter samples to operate at temperatures of 1900°C to 2000°C. These temperatures were projected as necessary for sufficient screen illumination from such a high work function surface.

The five basic components of the microscope are the sample mount and heater; the X, Y, and Z traverse mechanism; lenses; screen; and vacuum system. The design and operation of these components, especially the lens section, determine the quality of the image and the versatility of the instrument. Figure 10 is an assembly drawing of the modified microscope indicating the location of these components.

The emitter sample and electron bombardment heater assembly is an integral unit retained from the vacuum emission vehicle studies. It is therefore possible to transfer an emitter sample without intermediate steps of welding, brazing or processing from the VEV to the emission microscope. In this manner the sample surface remains free from distortion or contamination. It is also important to recall that the heater unit remains exactly in place with respect to the emitter, hence providing a means of reproducible temperature measurements.

Figure 10. Thermionic Emission Microscope, Assembly Detail

Sample temperatures were determined by measuring the temperature of a hohlraum drilled into the side of the sample with a depth-to-diameter ratio of 10 to 1. The hohlraum was observed through a view port located on the side of the vacuum chamber of the microscope. All temperature measurements were conducted with the same calibrated micro-optical pyrometer used to measure sample temperatures in the VEV. Corrections for view port losses were slightly less than the bell jar losses listed in Table I.

The sample mount and heater assembly are mounted on a 0.0001 inch micrometer drive X, Y, and Z traverse mechanism which provides a precision method for surveying the sample surface and for measuring the microscope magnification. Sample excursions of approximately 1/2 inch along the microscope axis and 3/8 inch in both directions perpendicular to the axis were possible.

The two electrostatic lenses, the immersion objective lens and the projection lens, are three-element lenses adapted from a design by Johannson and is discussed in detail in his paper (Ref. 9). Each lens is designed to yield an approximate magnification of 33X; therefore, the two lenses can achieve 1000X magnification. Since the image quality is extremely sensitive to the lens alignment and ellipticity of the individual lens apertures, the lens elements were assembled and aligned axially to within 0.0005 inch. The individual aperture ellipticity exceeded the design specification of 0.0004-inch roundness. The final alignment and inspections were conducted <u>after</u> the lenses were vacuum heat treated at temperatures 200 to 300°C higher than their intended temperatures of operation in the microscope.

Because of the high emitter temperatures and the close spacing between the grid and the sample, the first lens element intercepts a considerable amount of radiant heat. To avoid excessive heating of this element

and to reduce the possibility of warpage and misalignment, it is made from arc-cast molybdenum and mounted firmly on a heavy molybdenum ring which is in turn mounted firmly into the vacuum chamber walls. Because of this arrangement, the first lens element is necessarily operated at ground potential. The remaining four elements of the lenses are high voltage elements and are electrically insulated from the chamber. The last element of the projection lens is in contact with a cylindrical tube which supports a phosphor screen. This tube provides a field-free drift space and subsequent target area for electrons emerging from the lens system.

The phosphor screen simply converts the electron image to a visual image which is viewed through a 4-1/2 inch glass viewport in the end of the microscope chamber. The screen is a 3-1/4 inch diameter non-browning glass aluminized for 30 kV operation. It is coated with a P31 phosphor with a 1/8-inch hole in the center. In turn this hole is used to locate a precision hole insert of 0.040 ±0.0005 inch which serves as the aperture for electron emission measurements. Figure 11 is a sketch of the apparatus used to measure the electron flux through the screen aperture. It is commonly referred to as a **Faraday** cup or Faraday cage and was designed to permit emission measurements within the individual grains of vapor-deposited rhenium. This Faraday cup was installed with its axis concentric to the preceding lens system axis. The cup is also concentric to a decelerating collector which prohibits the formation of secondary electrons by way of high energy electrons from the voltage accelerating section (Ref. 10).

The cup current lead is guarded in such a manner as to compensate for the current meter voltage drop. A dc battery is used to equalize the potential across the holding ceramic, thus ensuring there are no potential differences that could cause small current shunts external to the measuring circuit.
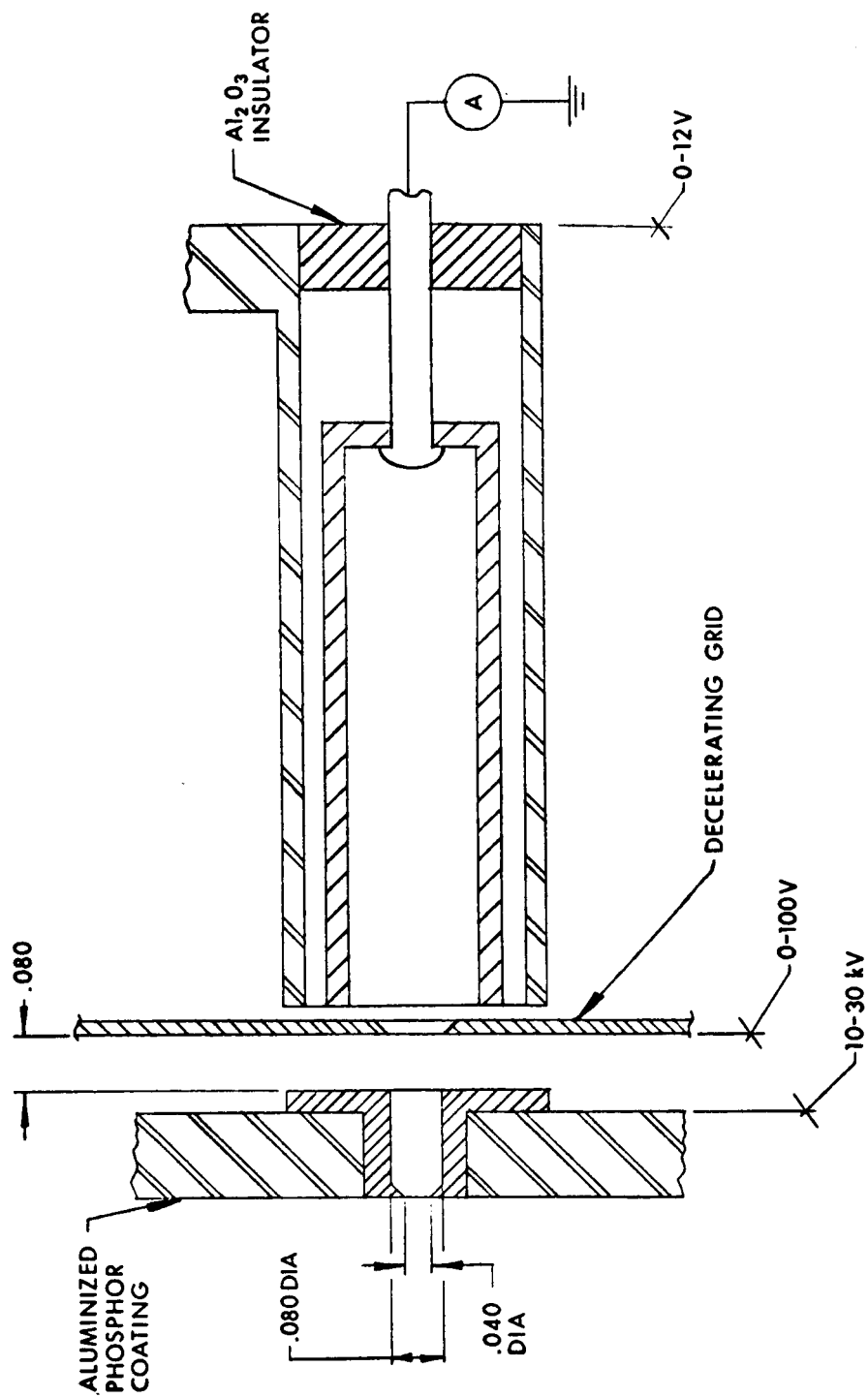
Figure 11. Faraday Cup Drawing

At current levels of 10^{-11} ampere and below, the problems of ac pickup and other electrical disturbances were minimized by electrically shielding and screening the meters and metering leads. The noise level measured 1 to 5 x 10^{-14} ampere at operating conditions.

The vacuum chamber was designed to be capable of ultrahigh vacuum operation. All components were fabricated of materials capable of high temperature vacuum processing. Copper gasket seals are used on all flanges and the seals of the view ports are fused-metal-to-glass seals. The entire unit may be processed at 400°C, although this temperature was not required in practice. It was found that a 200°C bakeout for six to eight hours was sufficient to obtain a pressure of 1 x 10^{-9} torr with a 140 liter/sec vac-ion pump. Since the presence of a 2 or 3 gauss magnetic field could disturb the electron beam trajectory in the low voltage section of the microscope, nonmagnetic stainless steels were utilized in the construction. Moreover, the vac-ion pump magnets were shielded with mu-metal. A gauss meter measurement in the microscope interior indicated a 0.15 to 0.25 gauss field (which is essentially the earth's magnetic field). Figure 12 is a picture of the microscope exterior.

All of the observations discussed in this report were made with the system evacuated to 1 x 10^{-8} torr and lower.

The thermionic emission microscope, in operation, satisfied or exceeded all the design goals. They are enumerated below.

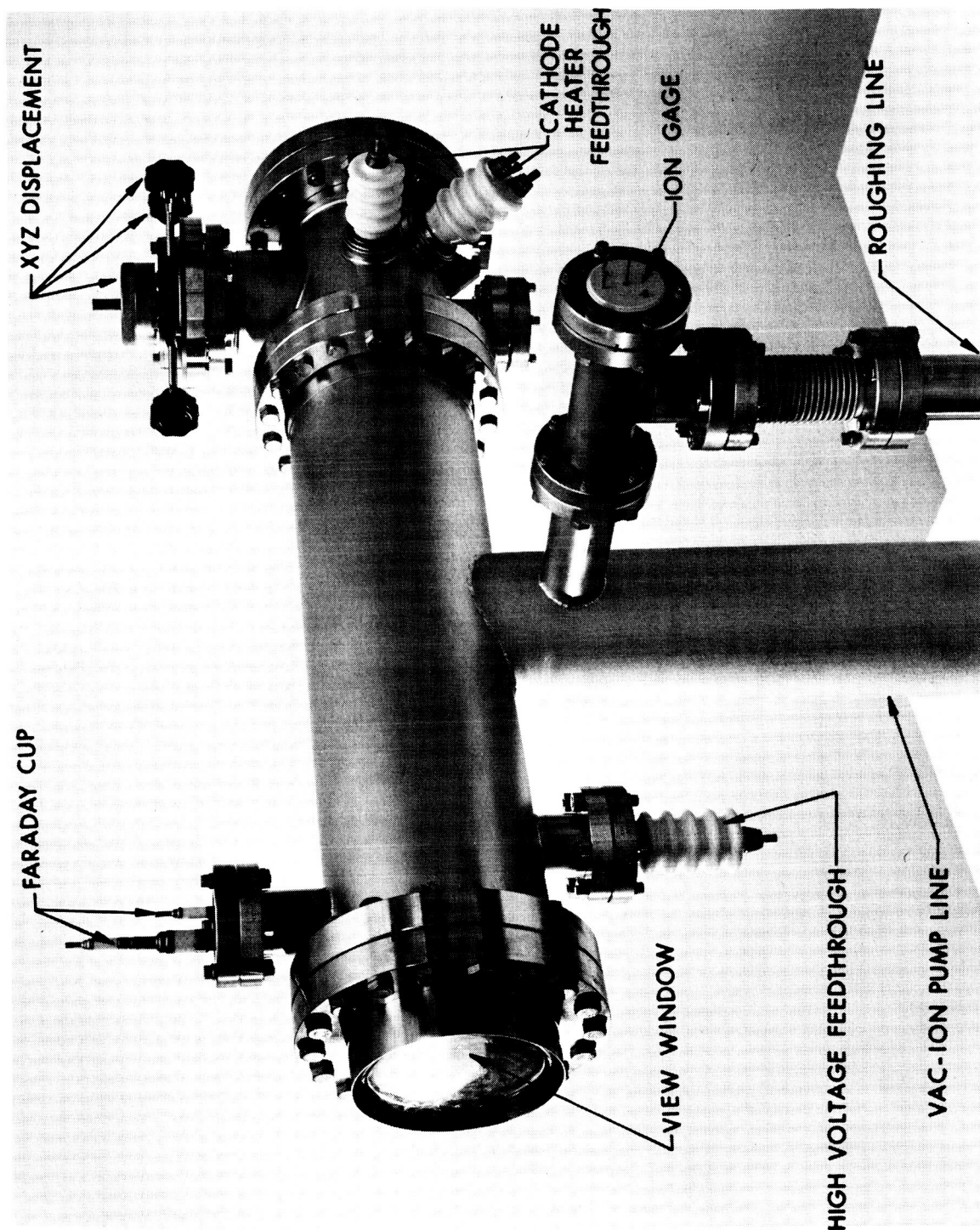|	
Magnification	Variable from 600 to 1400X
Resolution	Approximately 0.15 micron
High temperature operation	1900 to 2300°K (as measured by a micro-optical pyrometer sighted in a blackbody hohlraum)
Faraday cup	5 x 10^{-13} ampere and above

Figure 12. EOS Modified Microscope Assembly

Ultrahigh vacuum $< 1 \times 10^{-8}$ torr (at 2200°K emitter
                           temperature)

X,Y,Z traverse   Scans central 3 cm^2 of a cathode sample
mechanism   0.75 inch diameter

Figure 13 depicts the microscope in operation.

3.2 MICROSCOPIC INVESTIGATION OF VAPOR-DEPOSITED RHENIUM

Vapor-deposited rhenium sample II was selected for study in the ther-
mionic emission microscope. It represents an average sample of vapor-
deposited rhenium (with respect to thermal treatment, grain size, and
work function. This sample was transported directly from the vacuum
emission vehicle to the microscope and was operated almost immediately.

A randomly selected area of sample II was photographed, and a composite
picture of this area is shown in Fig. 14. The bright grain located in
the upper center of the picture is indicative of a low work function
grain surrounded by higher work-function grains (grey and black areas).
The dark center of each photograph is the hole insert of the Faraday
cage which was later mounted for emission measurements. Contrasting
shades between grains showing differences in work functions have been
observed previously, using thermionic emission microscopes. However,
work function differences <u>within</u> an individual grain (suggested by the
surface irregularities in Fig. 14) have not been observed.

Subsequently, the sample was diamond scribed with a set of orthogonal
axes which were used for identification and location of grains on the
sample surface. Figures 15a, 15c, and 15e are micrographs showing the
scribe marks as they originally appeared on the emitting sample sur-
face. It can be seen that the scribing operation work-hardened or
stressed the surface, which was subsequently recrystallized when the
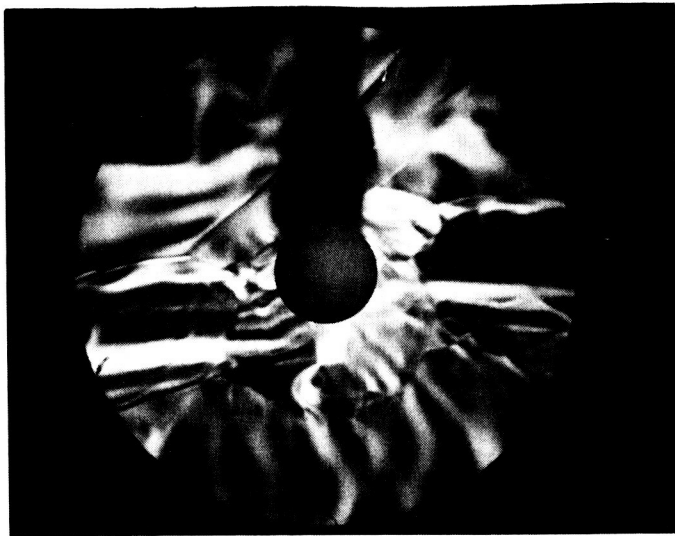emitter was brought to operating temperature. In some areas it is

Figure 13. Microscope Test Setup

Figure 14. Vapor-Deposited Rhenium Sample II Composite of
            Emission Micrographs (750X)
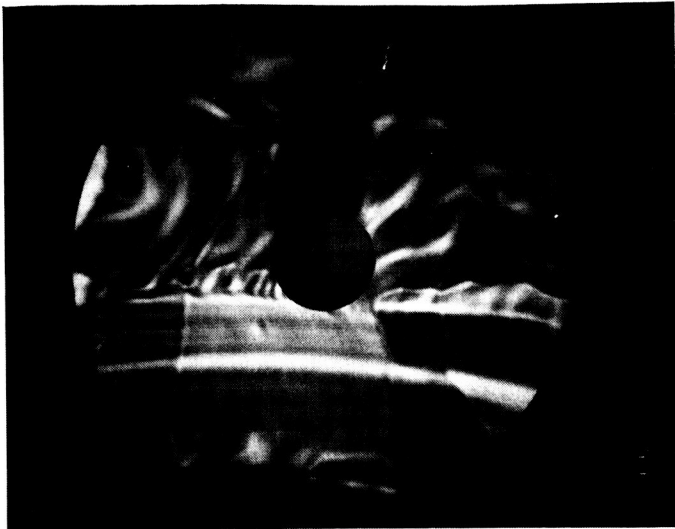
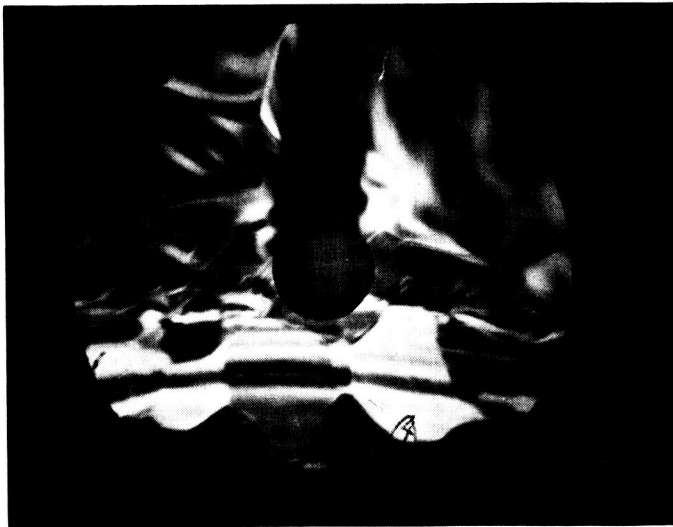a.   b.

c.   d.

e.   f.

Figure 15. Recrystallization History of Selected Areas Along a Scribed Surface Before and After Secondary (Preferential) Recrystallization of Vapor-Deposited Rhenium

interesting to note that this abrasion also exposed a more ordered surface, as evidenced in Fig. 15c wherein the surface irregularities have been "removed" from the dark grains.

Figures 15b, 15d, and 15f are photographs showing scribe lines after approximately 60 hours operation at 1800°C to 1900°C. These photographs show the lines have been totally stress relieved and that secondary or preferential recrystallization has taken place. This is consistent with emission microscope observations made on other materials such as molybdenum (Ref. 11). The central portion of the photograph is obscured by the Faraday cage which was placed in front of the screen aperture for emission measurements.

Figures 16 and 17 compare optical micrographs to the corresponding electron emission micrographs of the same locations on the sample surface. The optical micrographs contain a wider field of view and lack the field distortions at the picture edges which are apparent in the emission micrographs. On the basis of comparing several such corresponding sets of photographs, it was concluded that grains with similar microstructure and surface detail yield the same electron emission. It is worth noting that the surface structure observed in Fig. 16 was also identified as to form and quantity in the other three samples.

Figure 18 shows a surface irregularity typical of the sample. These irregularities are similar in appearance to chemical or dislocation "etch" pits observed on the surfaces of other materials. However, they lack the number density usually associated with such etch pits (Ref. 12). These irregularities are probably thermal etch pits -- a result of vacuum heat treatment.
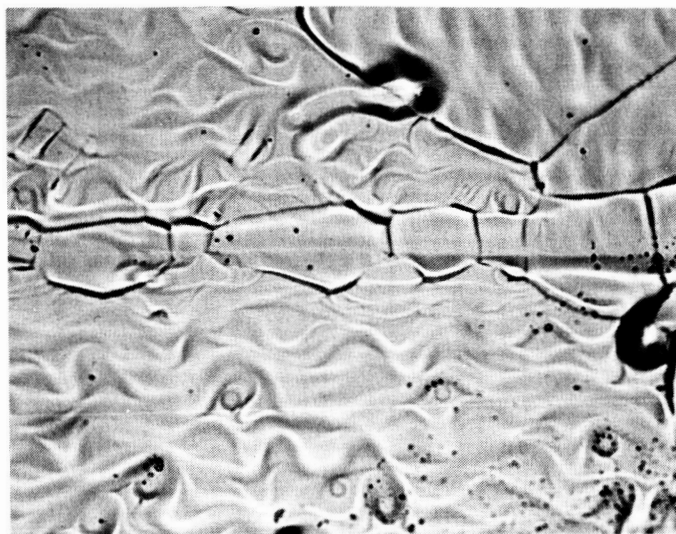
16a. Optical Micrograph

16b. Emission Micrograph

Figure 16. Micrographs of Vapor-Deposited
Rhenium, Sample II, at 1700°C
after Approximately 60 Hours of
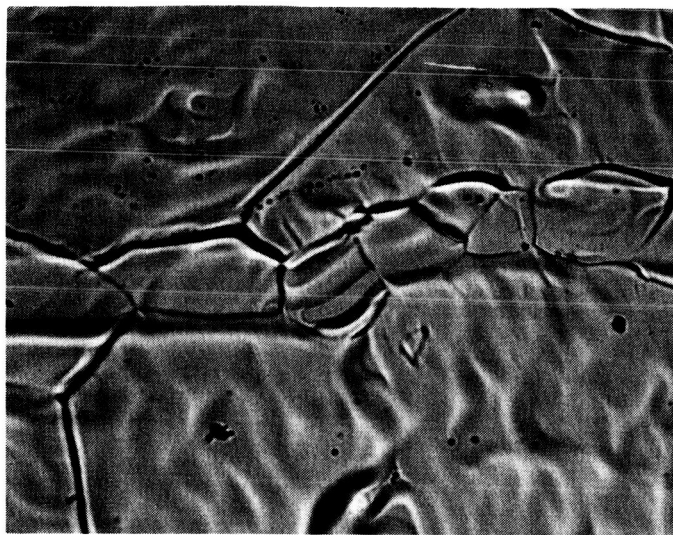Heat Treatment at Approximately
1850°C, (840X)

17a. Optical Micrograph

17b. Emission Micrograph

Figure 17. Micrographs of Vapor-Deposited Rhenium Sample II, at 1700°C after Approximately 60 Hours of Heat Treatment at About 1850°C (840X)

Figure 18. Micrograph of a Typical "Etch" Pit at 2000°K (1150X)

3.3 PREFERRED ORIENTATION OF VAPOR-DEPOSITED RHENIUM

The emission micrographs in the previous section have displayed an irregular surface which obviously is not characteristic of a single crystal material to ascertain the degree of preferred orientation exhibited by vapor-deposited rhenium.

A direct method utilizing a Geiger counter X-ray spectrometer (Ref. 13) was resorted to. An X-ray beam reflected from the sample surface was measured for a particular crystallographic plane as the specimen was rotated about an axis defined by the intersection of the sample surface and diffractometer axis. The variation of density of a particular plane as a function of angle, measured from the surface normal, indicated a strong texture.

Two vapor-deposited rhenium samples were evaluated: the first, as received in the vapor-deposit condition; the second with a prior outgassing heat treatment at 2300°C for three hours.

Table III shows the results of a simple symmetrical scan of the sample surface indicating the intensity of the various reflections. A very strong texture with the (002) planes parallel to the surface are seen.

Table IV shows the variation of density of (002) planes as a function of angle, measured from the surface normal. Table IV may be analyzed by assuming that the intensity is proportional to the volume of diffraction material, and calculating the volume of material within a given angle.

In sample I, 39.8 percent of the material is oriented with the (002) plane parallel to the surface and 82.8 percent is within 10 degrees of the surface. Sample II contains 29.6 percent with (002) orientation

TABLE III

SAMPLE SURFACE SCAN INTENSITIES

Sample I		Sample II	
hkl	I	hkl	I
100	3	100	5.5
002	100	002	100
101	25	101	4.4
102	6	102	2.2
110	0.5	110	~ 0
103	10	103	2.7
112	2	200	~ 0
201	~ 0	112	~ 0
004	10	201	~ 0
104	1	004	4.4
203	~ 0		
210	~ 0		

Cu $K\alpha$ radiation used

TABLE IV

DENSITY VARIATION OF (002) PLANES

Sample I		Sample II	
Tilt Angle	I	Tilt Angle	I
0	100	0	100
5	73	5	95
10	35	10	65
15	16	15	38
20	10	20	22
25	6	25	14
30	4	30	4
35	3	40	0.4
40	2.5		
50	2		

Cu $K\alpha$ radiation used

parallel to the surface and 77 percent within 10 degrees. There is
only a 5.8 percent decrease in (002) surface oriented material over a
10 degree tilt angle caused by the heat treatment. This gives a good
indication that vapor-deposited rhenium retains a high degree of (002)
texture.

The experimental analyses for this investigation were performed by
Prof. C. R. Barrett at the Stanford University Materials Science De-
partment in Palo Alto, California.

3.4 FARADAY CUP EMISSION MEASUREMENTS

Quantitative measurements of the emission from individual grains were
obtained by direct measurement of the electron current intercepted by
the Faraday cup located behind the screen aperture. The sample elec-
tron current density and the Faraday cage current can be related by
the first order equation

$$Jo = \frac{I \cdot M^2}{Ac} \tag{5}$$

where I is the current from the sample as measured in the Faraday cup,
Jo is the real emitter current density, M is the magnification of the
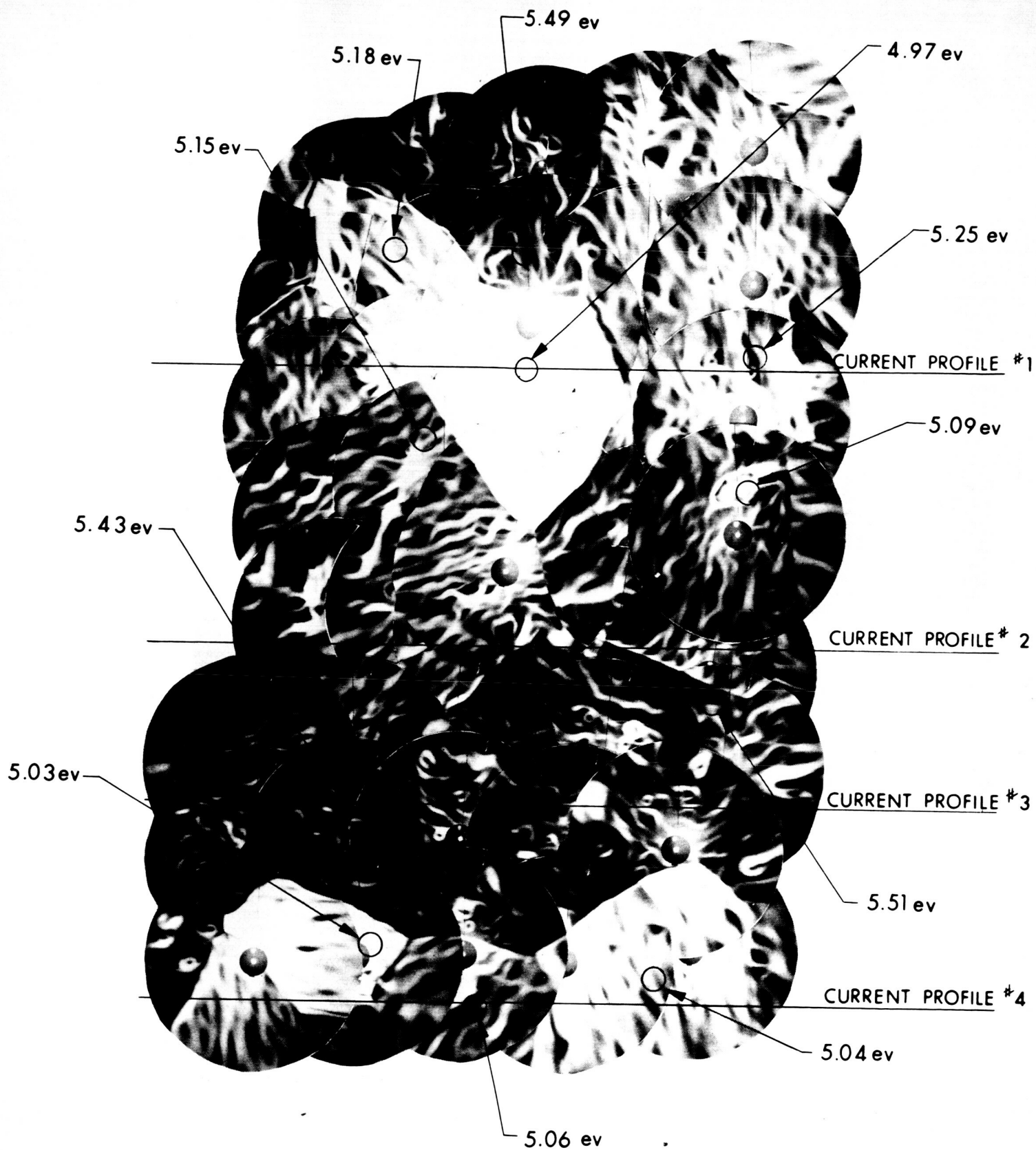microscope, and Ac is the area of the collecting hole in the center of
the screen.

A grid of 250 points was randomly selected from an area of 0.7 cm^2 and
examined for emission density. Three instruments were used inter-
changeably for measuring the current: a Keithly 610R, a Boonton 95A,
and a Cary 31. Measurements from the three instruments agreed within
± 1 percent. The Cary 31 is guaranteed to be within 1 percent accurate.

The average effective work function was computed by the direct substitution of the temperature and the emission current density into the Richardson-Dushman equation with A constant taken to be 120 A/cm^2/^{o}K^2. An average current value was obtained from 250 individual current measurements at an average emitter temperature of 2158°K. The average work function computed in this manner was 5.28 ±0.04 eV which compares to a value of 5.13 ±0.04 eV as obtained from the vacuum emission vehicle. The apparent disparity between these values can be attributed to the fact that the surface of the vapor-deposited sample is so irregular that ten to a hundred times more Faraday cup measurements might be required to obtain a more nearly true average value for the work function.

The effective work functions of the indicated areas on a previously mapped composite of a sample area are shown in Fig. 19. There is a wide variation of ϕ_{eff} (4.97 to 5.52 eV) exhibited by the individual grains, but the lowest of 4.97 eV is approximately 80 to 100 mV higher than polycrystalline rhenium while the highest work function approaches that of single crystal rhenium of the (0001) orientation.

To better delineate the variation of emission associated with the irregularities displayed by the surface, current profiles were taken. By recording the current on a calibrated X-Y plotter, a graphic presentation of the high and low emission areas can be shown. The axes and their emission profiles measured are also shown in Fig. 19. This graphic technique substantiates that the emission is high in the light regions and low in the dark regions. Also, it indicates that there are regions of high emission in predominantly dark areas that are on the order of 0.0001 inch or less in width.
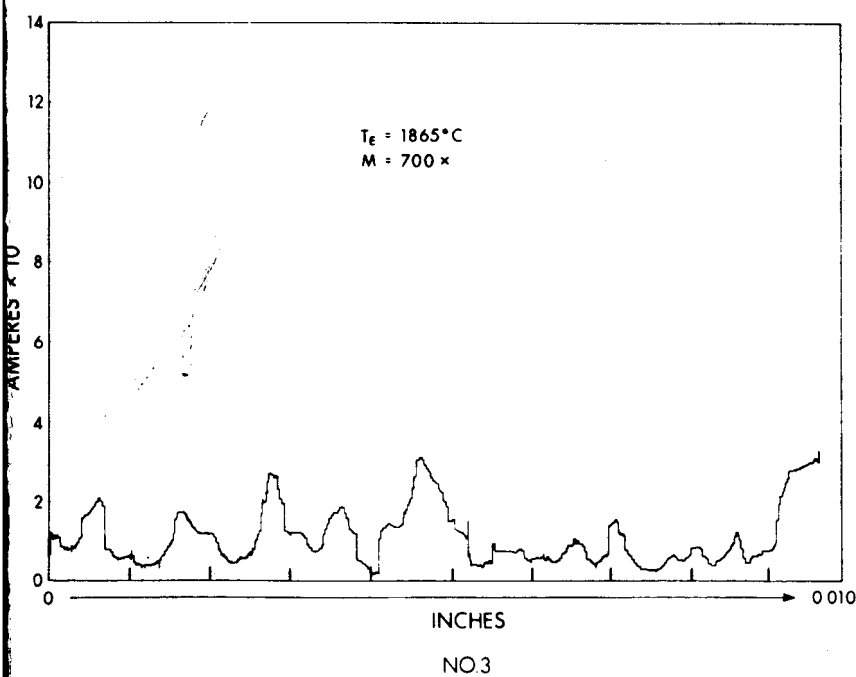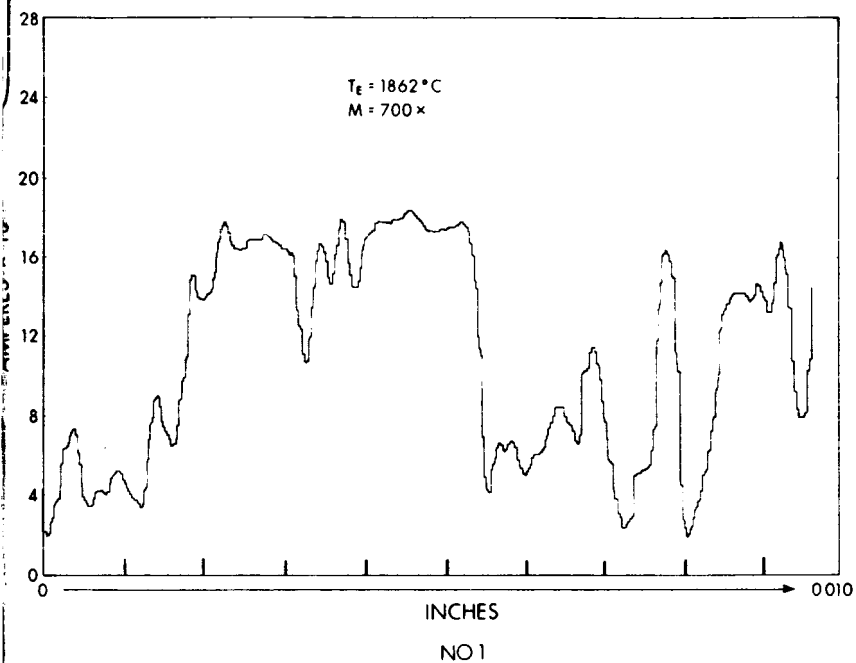
A typical emission profile comparing two magnifications is shown in Fig. 20. This technique of emission profiles has been used by other investigators, such as D. Schnek in 1935 (Ref. 14).

5.49 ev

5.18 ev

4.97 ev

5.15 ev

5.25 ev

CURRENT PROFILE #1

5.09 ev

5.43 ev

CURRENT PROFILE #2

5.03 ev

CURRENT PROFILE #3

5.51 ev

5.04 ev

CURRENT PROFILE #4

5.06 ev

P0306

7118-SA-2

45

NO 1

$T_E = 1862°C$
$M = 700×$
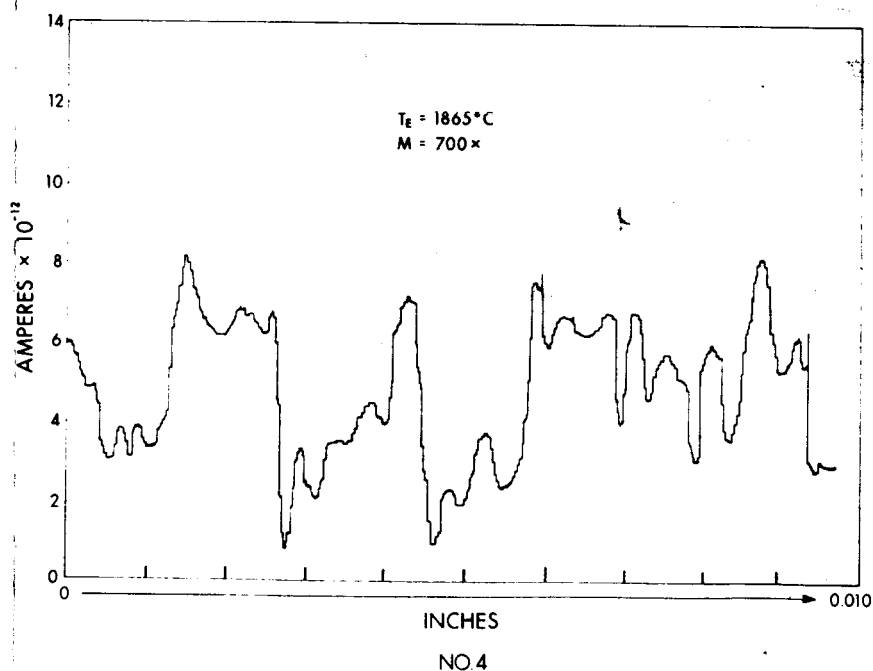

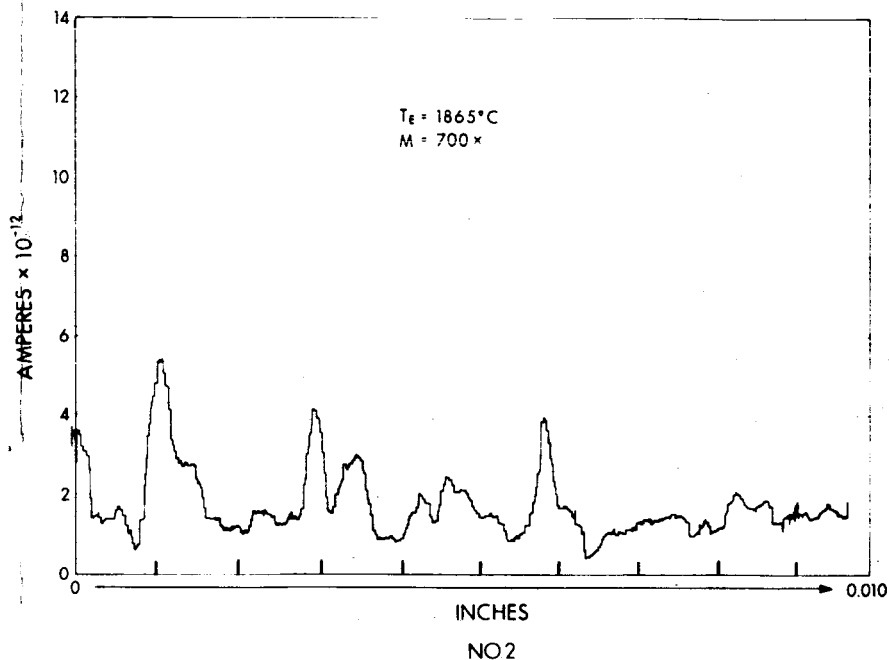NO.3

$T_E = 1865°C$
$M = 700×$

46-1

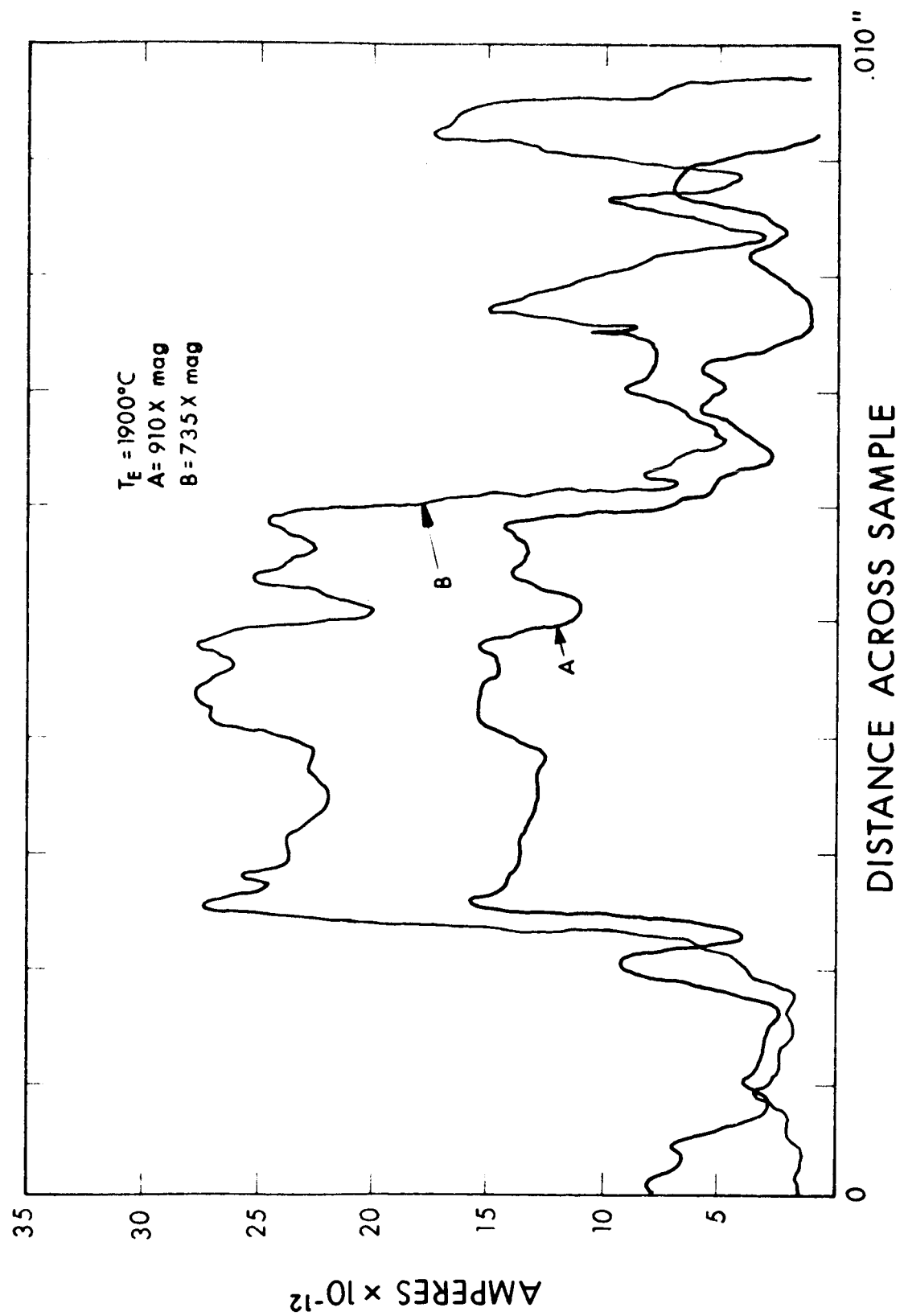Figure 19. Mapped Composite of Sample Area with Current Profiles

46-2

Figure 20. Emission Profiles Before (A) and After (B) Electro-Etching

3.5 MICROSCOPE OBSERVATIONS ON VAPOR-DEPOSITED RHENIUM SAMPLE II AFTER ELECTRO-ETCHING

Vapor-deposited sample II was electro-etched by methods as described in Section 2. A composite of the microstructure after etching is shown in Fig. 21.

The electro-etching carved wider and deeper grain boundaries. The light areas showed signs of intense attack, while dark areas were only slightly etched. Etch pits were deeper and some areas were darker.

Emission profiles were taken across the sample and graphic analysis was made to determine if there was any change in the average emission characteristics of the sample. Figure 22 compares the emission profiles before and after electro-etching. The analysis showed that the average emission had not changed, although there were changes in the characteristics of individual grains; in some grains the emission was decreased, where in others the emission increased, but the overall characteristic was the same.

Figure 21. Composite After Electro-Etch of Mapped Area (12 mil square)
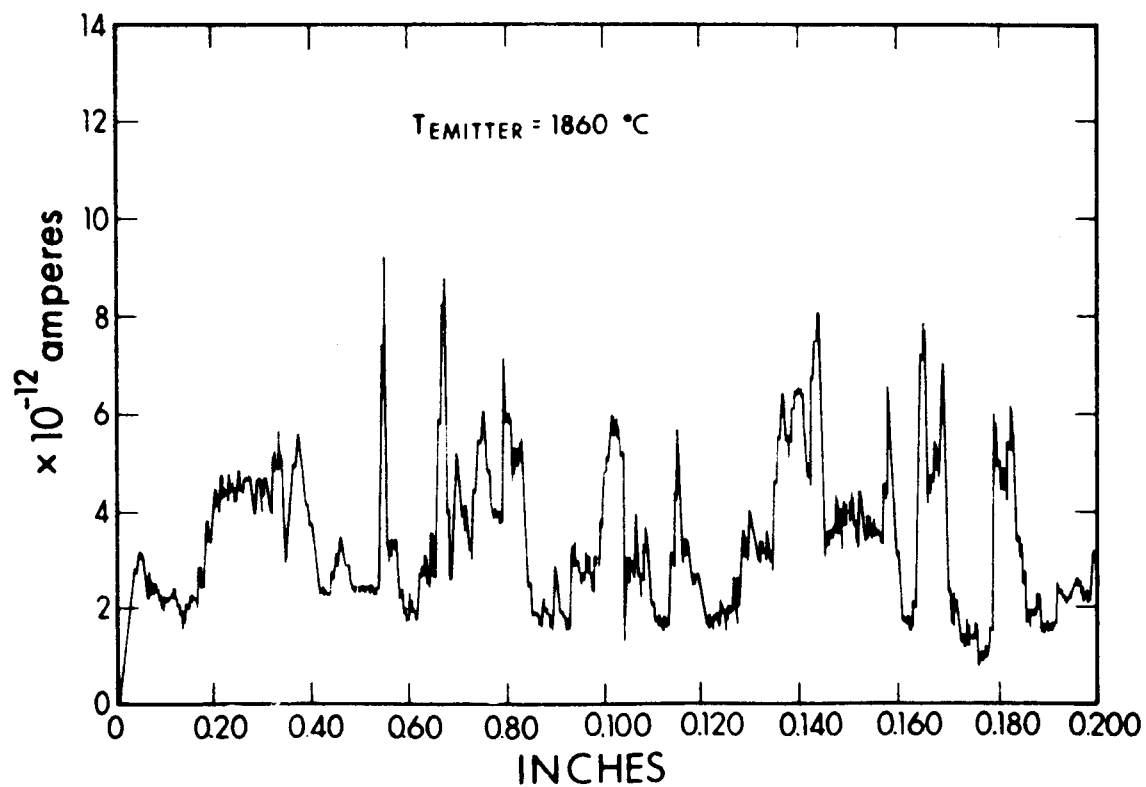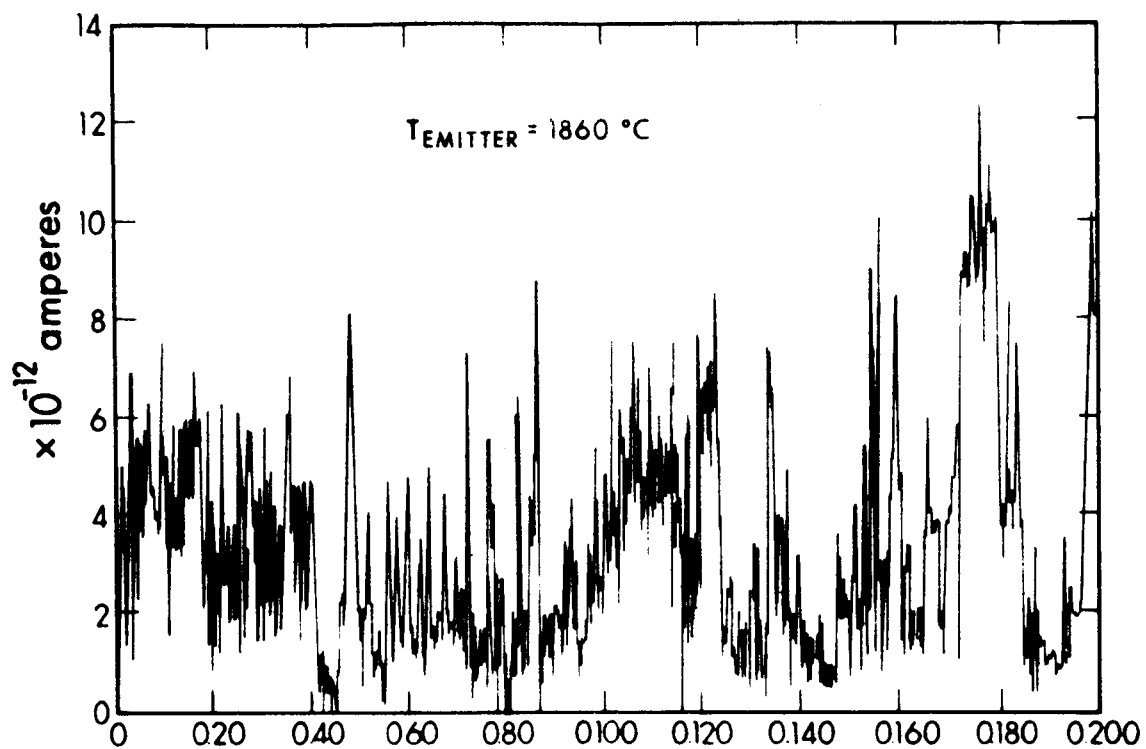
Figure 22. Emission Profile, Before and After Electro-Etching

SECTION 4

ANALYSIS AND INTERPRETATION (TASK III)

4.1 INTRODUCTION

The primary objective of this analysis is to formulate a theoretical description of thermionic converter performance and apply it to an analysis and correlation of the parametric vehicle data. Specific topics receiving attention are: (1) the similarity laws of a cesium vapor discharge, (2) the ionization mechanisms in a cesium plasma, and (3) the characteristics of the collector sheath. The analysis will attempt to cover each region of parametric vehicle operation as defined by the typical output voltage interelectrode spacing curve, V(d), shown in Fig. 23.

Region I of Fig. 23 is designated the electron space charge region and extends from zero interelectrode spacing to the minimum of V(d) identified as the plasma onset point. In region I, the output voltage at small interelectrode spacings is governed primarily by space charge created by electrons emitted by both emitter and collector in the absence of significant numbers of cesium ions. The theoretical model adapted for the first analysis of this region is the double vacuum diode. This model is valid at very small spacings but requires correction as the onset point is approached, for it is here that collisions and/or absorption of radiation create excited atoms and positive ions (probably molecular) of cesium.

For interelectrode spacings at the plasma onset point and above, the voltage output curve begins to display characteristics of a cesium plasma diode. For this reason, region II between the plasma onset
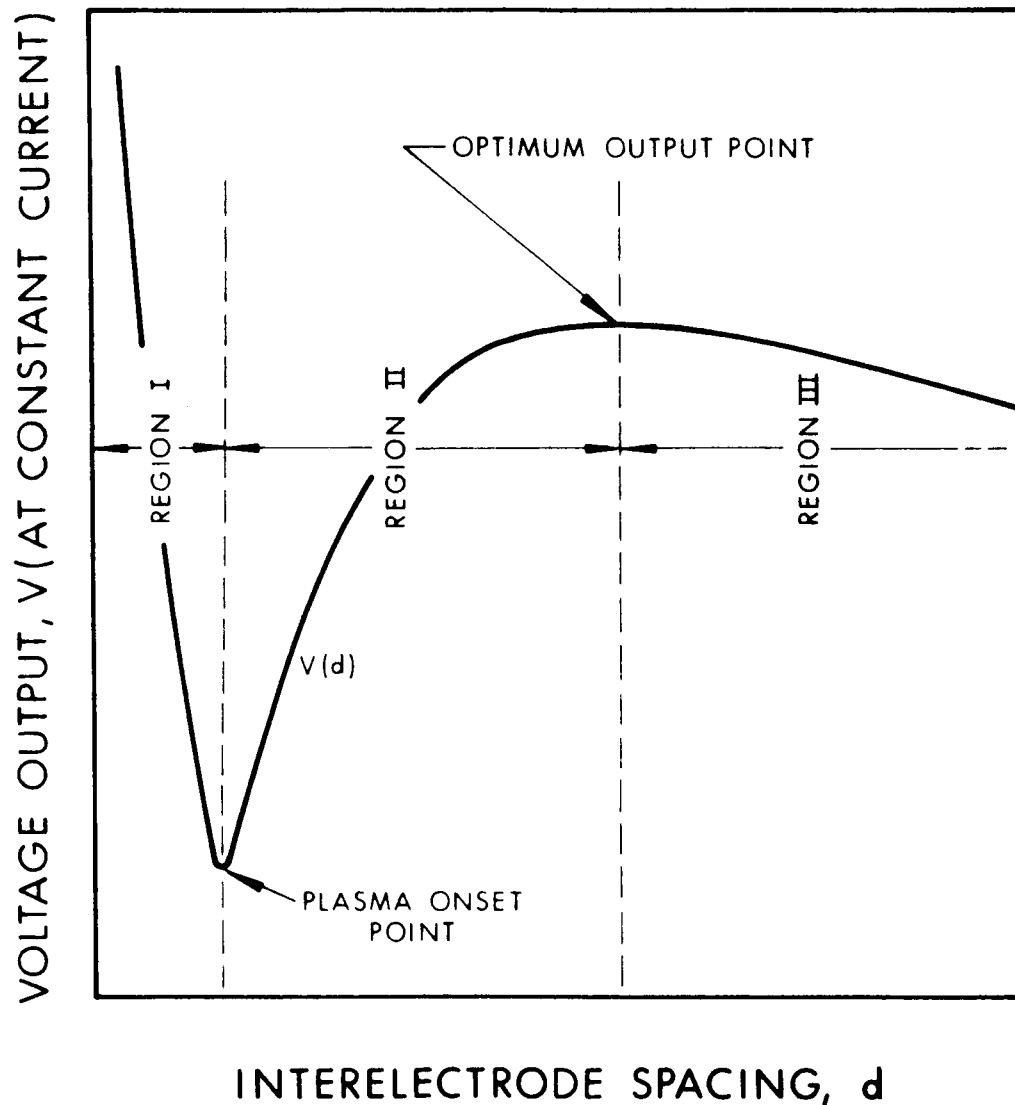
Figure 23. Typical Voltage Output versus Interelectrode
            Spacing Curve Showing the Three Characteristic
            Regions Described in the Text

point and the maximum of V(d) (identified as the optimum output point in Fig. 23) is designated the transition region. It is in this region that the plasma becomes fully developed. Region III is defined by the remaining portion of the output curve beyond the optimum power point and is designated the positive column region.

An analysis of the electron space charge region has been completed with a machine solution which relates output voltage to interelectrode spacing. The theory of the vacuum double diode was formulated previously and is not repeated here, rather the computer solution, its limitations, and comparison with experimental results are discussed.

4.2 COMPUTER SOLUTIONS OF POISSON'S EQUATION FOR THE DOUBLE DIODE

Poisson's equation for the double diode was derived in Ref. 1 and is repeated here for reference.

$$\frac{d^2\eta}{d\xi^2} = e^{\eta}\left[1 \pm \text{erf}\,(\eta^{1/2})\right] + \beta e^{\alpha\eta}\left[1 \mp \text{erf}\,(\alpha^{1/2}\eta^{1/2})\right] \quad (6)$$

where the positive and negative signs are for $\xi \lessgtr 0$.

Experience in use of the computer program for solutions of this equation has led to improvements in the program and a better understanding of the physics involved. The improvements will be discussed as they relate to the computer program sequence given in the previous reports.

Completed solutions provide information on the initial value to guess for β with a given set of chosen parameters. This minimizes the number of iterations necessary to find a solution. The computed electrode spacing ($\xi_c - \xi_e$) was found to vary almost linearly with log β. Therefore, the second trial value of β is found by multiplying or dividing

the initial value by a chosen constant. When two iterations are complete, each succeeding trial value for β is found by extrapolation or interpolation using the previous two values of β and the resultant computed electrode spacings. The logarithmic variation of β is used in the predicting equation.

There are upper and lower limits on the electrode spacing which may be used in this analysis of a space charge limited thermionic double diode. These limits are determined by the choice of current density in the diode, the electrode surface temperatures, and work functions, which are held constant for each computation.

For discussion of the lower limit on diode electrode spacing we need two equations not explicitly given in the previous report. They are the relationship of normalized electrode potentials to the other parameters:

$$\eta\Big|_e = \ln\left[\frac{2^2 \pi m k^2}{h^3} T_e^2 J\left(1 - \frac{\beta}{\alpha^{1/2}}\right)\right] - \frac{e\phi_e}{kT_e} \tag{7}$$

and

$$\eta\Big|_c = \frac{1}{\alpha}\ln\left[\frac{2^2 \pi m k^2}{h^3} \frac{T_c^{3/2} T_e^{1/2}}{}\left(\beta^{-1} - \alpha^{-1/2}\right)\right] - \frac{e\phi_c}{kT_e} \tag{8}$$

The minimum useful electrode spacing for analytical purposes occurs when the collector moves so close to the emitter that its position coincides with that of the space charge potential minimum. It may be observed from Fig. 24 that increasing β decreases the distance between given potential values. Since the normalized collector potential also decreases as β is increased, the maximum allowable value for β may be calculated by solving Eq. 8 for β and allowing the collector potential to approach zero. There is a related higher limit on **β** set by Eq. 7 but Eq. 8 gives the smallest value since the emitter temperature is higher than the collector temperature. If a chosen electrode spacing
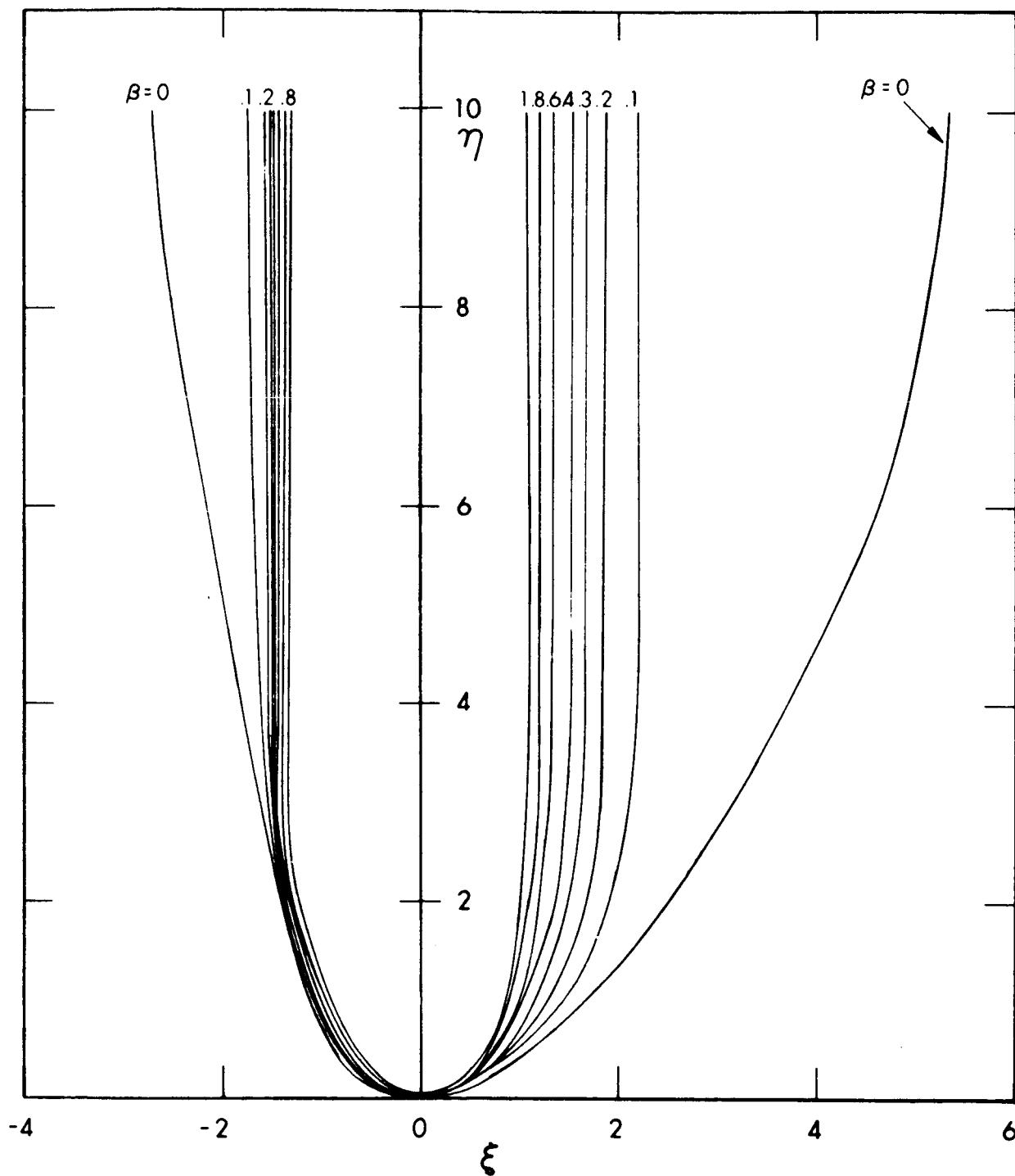
Figure 24. Normalized Potential Distribution (η) versus Normalized Coordinate (ξ) in the Interelectrode Space for the Case of $\alpha = 1.94364$ and Several Values of β (α and β are defined in the text)

is too small in relationship to the other parameters, the computer program will sense the second try of the maximum β (for $\eta/c = 0$) and print a message stating that the spacing is too small, and then proceed to try the next set of data.

The maximum emitter-to-collector spacing for a given set of chosen parameters of the space charge limited diode is determined by available input energy. As the spacing approaches the upper limit, the required applied potential increases rapidly. From Fig. 24 it will be noted that $\beta = 0$ gives the largest spacing between given potentials. From Eq. 6 it will be noted that as β approaches zero, the relationship between potential and distance becomes independent of α. The approximate value of maximum normalized spacing may be obtained from Fig. 25. It will be noted that the left branch becomes essentially vertical at $\xi_e = -2.9$ and the right branch becomes essentially vertical at $\xi_c = 5.5$. The normalized spacing thus given is $\xi_d = 8.4$.

The Debye length for normalization of the chosen distance includes β as a variable:

$$\lambda = \left[\left(\frac{\epsilon_o k^3 2^{1/2}}{e\, m^{1/2}} \right) \frac{T_e^{3/2}}{J} \left(1 - \frac{\beta}{\alpha^{1/2}} \right) \right]^{1/2} \tag{9}$$

Fortunately, as β approaches zero (in the case of large electrode spacing) λ becomes independent of β. In the computer program, the normalized value of the chosen distance is compared with the fixed value 8.4. If the chosen distance is too large, a message stating that fact is printed and the next set of parameters is tried. Of course, the presence of ions in the practical diode will tend to neutralize space charge effects allowing larger spacing of the electrodes. The effect of ions could be included in future models of the computer program.
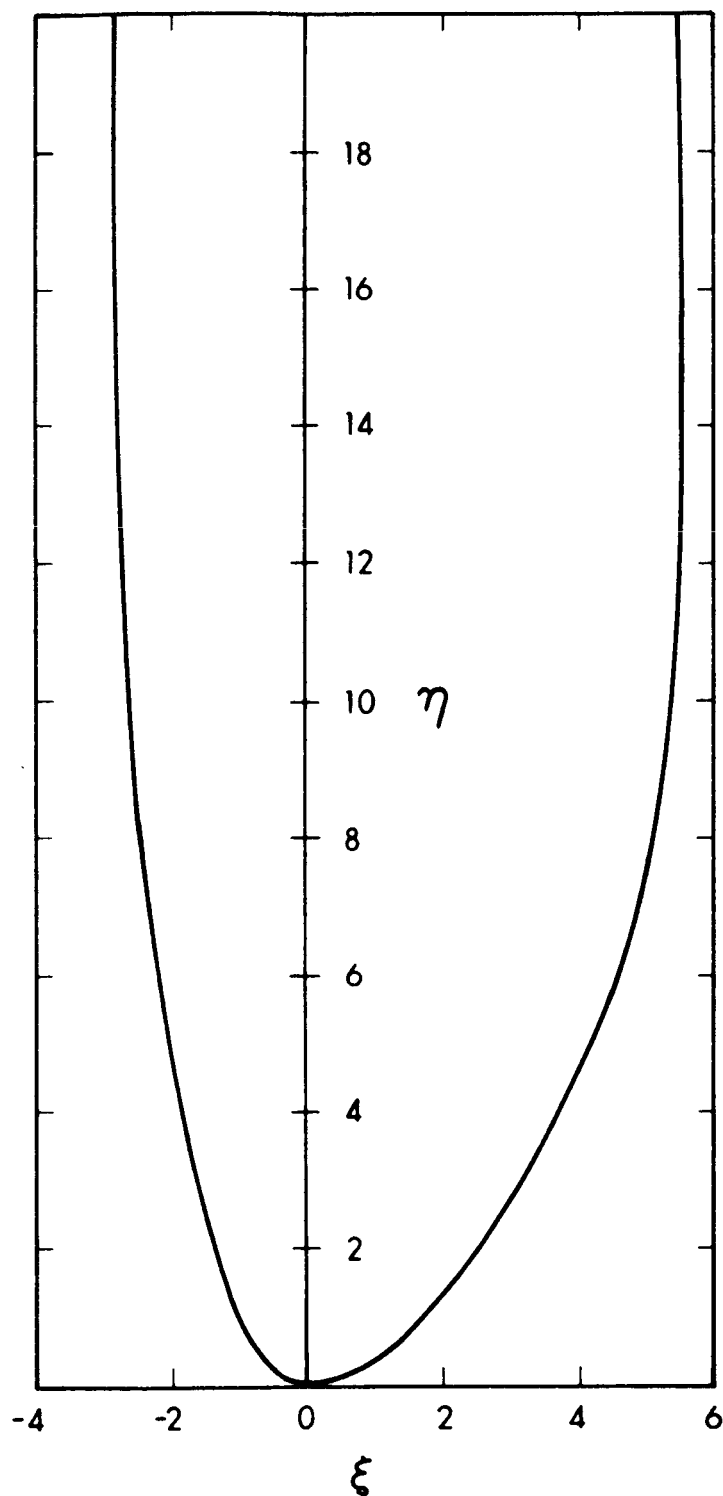
Figure 25. Normalized Potential versus Normalized
Distance in the Interelectrode Space
for $\beta = 0$ (β is defined in the text)

The comparison of computed results with experimental results is given in Fig. 26. The discrepancy in output voltage at low spacings is related to losses in lead resistance between the electrode surfaces and the point at which potential was measured. It is expected that the small amount of ionization present would make the slope of the experimental curve less steep than the theoretical curve for a vacuum diode. The degree of agreement between theory and experiment gives sufficient encouragement for future work on the computer program.
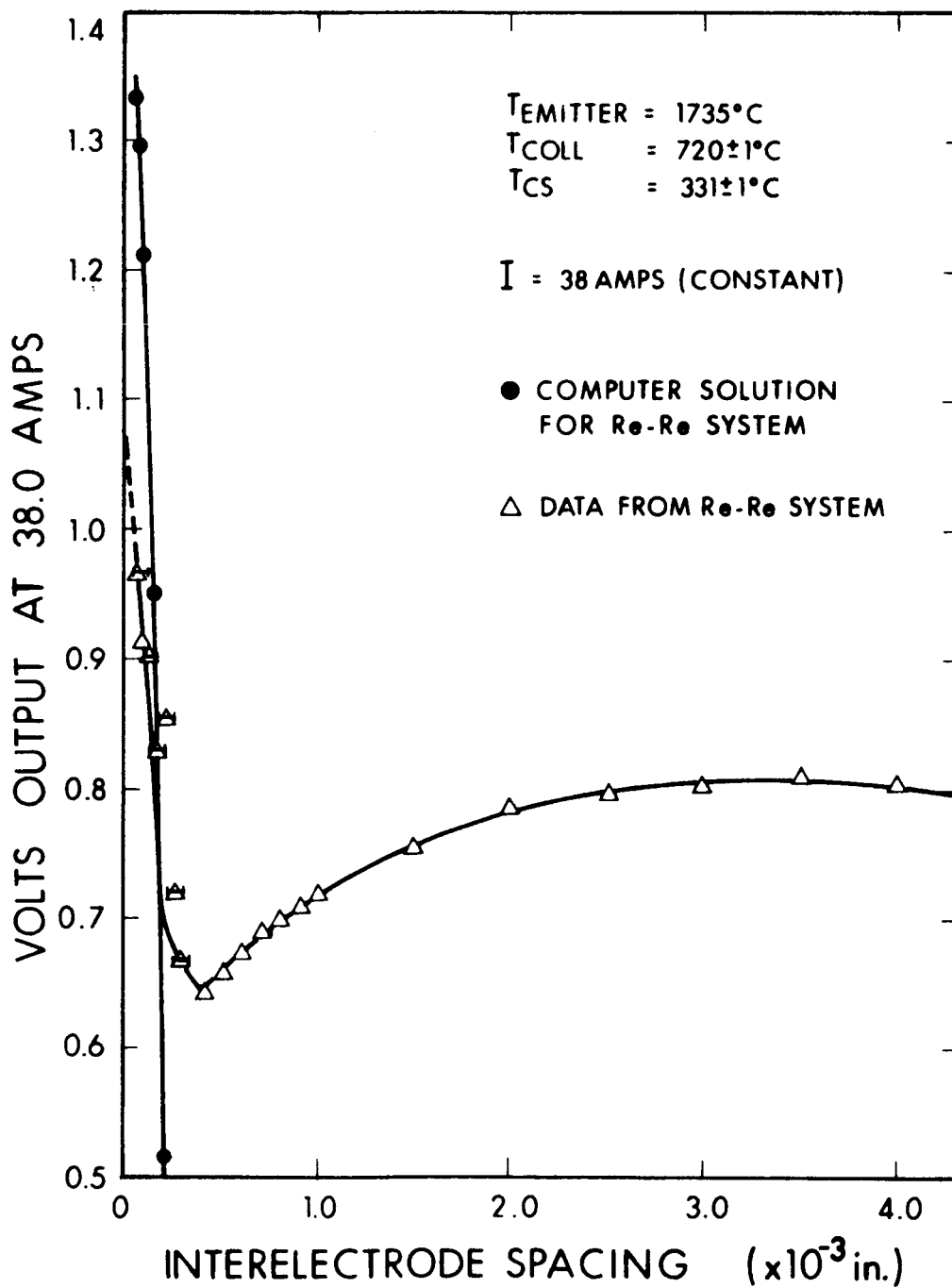
Figure 26.   Comparison of Computed Results with Experimental
            Results

REFERENCES

1. First Semiannual Report of Progress, "Thermionic Research and Development Program," Contract NAS7-514, 4 February 1967

2. Ibid. p. 41

3. S. Dushman, "Thermionic Emission," Rev. Mod. Phys., 2 (1930)

4. C. Herring and M. H. Nichols, "Thermionic Emission," Rev. Mod. Phys., 21 (1949)

5. W. Schottky, "Theory of Thermionic Emission," Physik, Z. 38 (1937)

6. H. J. Kostkowski and R. D. Lee, Theory and Methods of Optical Pyrometry, National Bureau of Standards Monograph 41, p. 24.

7. E. Guth and C. J. Mullin, Phys. Rev. 59, 575 (1941)

8. E. A. Coomes and I. J. O'Haenens, The Use of Precise Schottky Data in the Analysis of the Metal-Vacuum Surface Barrier for Thermionic Emitters, I-Rhenium, Report AFCRL-67-0189, 1967

9. H. Johannson, Ann. Phys. 18, 385 (1933) and 21, 274 (1934)

10. K. Spangenberg, Vacuum Tubes, McGraw-Hill, New York, 1948

11. A. O. Jensen, Research Program Related to Vapor Thermionic Converters for Nuclear Application, Electro-Optical Systems, Final Report, NASA Contract 3-2529

12. L. C. Lovell, J. H. Wemmick, "Dislocation Etch Pits and Polygonization in High Purity Copper," JAP, 30, 4, p. 390 (April 1959)

13. L. G. Schulz, J. App. Phys. 20, 1030-33 (1949)

14. D. Schnek, Ann. der Phyzik, (1935)